ADVANCES IN MEASURING PARAMETERS OF THE AIR-VOID SYSTEM IN HARDENED CONCRETE

BY

RUOFEI ZOU

THESIS

Submitted in partial fulfillment of the requirements
for the degree of Master of Science in Civil Engineering
in the Graduate College of the
University of Illinois at Urbana-Champaign, 2014

Urbana, Illinois

Adviser:

Professor David A. Lange

Abstract

To improve the freezing and thawing resistance of concrete, air bubbles are entrained and distributed evenly and closely. Evaluation of the parameters of the air-void system in hardened concrete is detailed in ASTM C457 "Standard Test Method for Microscopical Determination of Parameters of the Air-Void System in Hardened Concrete." Microscopical methods are used to determine traverse lengths of air voids, aggregates, and pastes on the polished surface of concrete samples. Since this manual measurement is time-consuming, tedious, and dependent on skills of operators, automated methods are preferred. This study recommends improvements to both the ASTM C457 test protocol and the metrics that are used to characterize the air void system.

A flatbed scanner is used to acquire a single high resolution image of the polished surface of a concrete sample. The concrete surface is polished and treated with phenolphthalein and orange powder to facilitate segmentation of air bubbles, paste and aggregate phases. The image is processed using ImageJ, Photoshop, and Matlab software. A three-phase image is generated with air, paste, and aggregate phases shown in white, gray, and black, respectively. Using the three-phase image, ASTM C457 parameters can be readily determined by computer.

To validate the new approach, six groups of concrete samples were examined in a "blind study." The concrete samples were donated by CTLGroup which had previously evaluated the air void system using the standard ASTM C457 test method. A good agreement between the two methods was shown except in the case of samples with lightweight aggregates.

The mechanism of freezing and thawing damage is complicated and theories proposed by researchers cannot explain all the observations or establish a clear relationship between the

spacing of air void, the freezing rate and the paste properties. In many respects, these theories complement each other. Air entrainment is effective and reliable to resist freezing and thawing for concrete designed for outside exposure in the cold climate. The structure of the air-void system is critical for the frost resistance of concrete and the spacing factor is one of the most significant parameters of the air-void system.

A new approach to spacing factor is developed in this study using two-dimensional images to provide better information than linear traverse or point count methods. The average distance of pastes to the nearest air void, the percentage of protected pastes, the area fraction of air voids, and the surface area of air voids are two-dimensional parameters which can be used to evaluate the freezing and thawing performance considering the physical properties and the mechanism of freezing of concrete. A comparative study is conducted between the two-dimensional parameters and the one-dimensional parameters in ASTM C457 and the advantages of the two-dimensional parameters are presented.

Acknowledgement

I would like to thank my advisor, Prof. David A. Lange, for his guidance and support in this project. I would also like to thank Yu Song and Daniel Castenada who helped me throughout this project. I learned a lot from them.

I would also like to thank the Federal Railroad Administration for their support in my MS program and for the opportunity to participate in the research project on freeze-thaw performance of concrete cross ties. I also appreciate CTLGroup for their providing concrete samples and the laboratory tour.

Table of Contents

Chapter 1. Introduction

Hardened cement paste, a porous material, is susceptible to frost attack under repeated cycles of freezing and thawing. Moisture contained in the concrete contributes to the damage and concrete may be destroyed in winter in the cold climate. Typical signs of freezing and thawing damage are spalling and scaling of the surface, exposing of aggregates, surface parallel cracking and gaps around aggregates.

Fortunately, concrete can be made to resist freezing and thawing by the addition of air-entraining admixtures that increase the amount of air incorporated into concrete. For field practices, an air content in the range of 2 to 8% by volume of concrete is appropriate for frost resistance and the actual amount depends on the maximum size of the coarse aggregate [1]. Air-entraining admixtures contain compounds that will promote the formation of stable foams. Since the high surface tension of water hinders the creation of the air-water interface, bubble formation is normally a transient phenomenon. Surface-active agents in air-entraining agents that concentrate at the air-water interface could lower the surface tension so that bubbles are stabilized. Surface-active agents are molecules that at one end have chemical groups that tend to dissolve in water (hydrophilic), while the rest of the molecule is repelled by water (hydrophobic) [1]. The air entraining admixtures cause the water to foam and the bubbles are stabilized in the paste.

The entrained air is bubbles that are uniformly distributed in the pastes and the air system plays an important role in improving freezing and thawing performance. The water in the capillary and gel pores in the pastes can expand into the air voids when the concrete is exposed to the freezing condition. The internal pressure generated in the pastes can then be decreased and the freezing damage is alleviated.

The most commonly used method to evaluate the air void system is ASTM C457 “Standard Test Method for Microscopical Determination of Parameters of the Air-Void System in Hardened Concrete (ASTM C457), which measures the parameters of the air-void system along straight lines on the polished concrete surface [2]. Optical equipment is utilized to determine the traverse length of air voids, aggregates, and pastes. Other parameters including specific surface, void frequency, and spacing factor can be calculated based on the air voids, aggregates, and pastes portion and the number of traversed air voids. However, these measurements require manually tedious and time-consuming work. The quality of the optical measurement depends on the skills and experience of operators. Moreover, since the evaluation is based on the measurement along straight lines, the three-dimensional true properties are predicted by one-dimensional parameters. Therefore, some errors should be expected in the evaluation of the freezing and thawing performance.

Automated methods to conduct ASTM C457 have been the subject of research for many years, striving to overcome those disadvantages by collecting and analyzing an image of the polished surface with reduced labor. The image could be collected by a camera attached to an optical microscope [3, 4, 5] or by a scanning electron microscope (SEM) [6]. These methods enhance the contrast by painting the surface black and filling the air voids with white powder. One of the disadvantages is that after the treatment, the aggregate fraction and the paste fraction cannot be differentiated automatically, requiring that multiple images of one surface are typically required. A flatbed scanner has also been used to acquire the image [7, 8]. This method, developed by Peterson et al., determines the paste fraction, which is an essential parameter to compute the spacing factor according to ASTM C457. Peterson further advanced this method and applied in some practical work [9, 10, 11]. Other researchers have also verified the advantages of the

automated method using flatbed scanners [12, 13, 14, 15]. Three scanned images are aligned to yield an output image including the original surface, the surface stained with phenolphthalein to pink the paste, and the surface painted by black with air voids filled with white powders. Although the superposition of these images could detect the fraction of aggregates, paste, and air voids, the scanning process still needs high quality of workmanship and three-time scanning is still cumbersome in practice.

Advances in measuring the parameters of the air-void system are proposed in the study. The method presented here requires only a single high resolution image acquired using a high resolution flatbed scanner (4800 dpi). Before scanning, the surface is polished and treated with phenolphthalein to render the paste a pink color. The air voids are then filled with orange powder to provide for tonal contrast. The scanned image is processed using ImageJ, Photoshop, and Matlab to segment the air voids, aggregates, and pastes automatically.

In order to verify the applicability and the accuracy, the comparison will be conducted on the same parameters of the air-void system with the results according to ASTM C457 provided by CTLGroup. The difference between microscopy-based linear traverse method in ASTM C457 and the automated scanning method will be shown in detail in Chapter 2. For the kind of method, the measurement can be extended to two dimension and new two-dimensional parameters can be proposed to evaluate the freezing and thawing performance.

The parameters of the air-void system are expected to represent the true nature during freezing and hence, it is necessary to revisit the mechanism of freezing. Researchers have suggested various competing theories in the last 60 years about the mechanism of freezing action in hardened concrete. Although the early hypotheses are considered to be incomplete, they have

provided the basis for the continued study of frost action in concrete. At first, the expansion of water by 9% of its original volume during freezing was noted to explain the freezing process. Very simply, water in saturated pores in concrete expands, creates stress, and causes cracking. This theory was soon recognized as not entirely satisfactory and other theories were put forward such as hydraulic pressure theory by Powers [16], energy of solidification theory by Helmuth [17], osmotic pressure theory by Powers and Helmuth [18], and Litvan theory [19]. Besides these classical theories, Chatterji [20] explained how ice forms in the air bubbles and the specific effect of different air-entraining admixtures, which depends on the different hydrophobicity. Crystallization pressure is also shown to be the reason for freezing damage in many situations by Scherer and other researchers [21]. Cryo-suction effects are then modeled by Monteiro based on the unsaturated poroelasticity theory and the air voids are shown to act as both expansion reservoirs and cryo-pumps [22].

As the most referred freezing mechanism, Powers hydraulic pressure theory provides an order of magnitude for the freezing stress and determines the critical spacing factor. However, some questions and criticisms have put forward for the mechanism and model. It is necessary to revisit Powers hydraulic pressure theory and determine if it is reasonable to use the spacing factor in evaluating the freezing and thawing performance. The mechanism of freezing action and the critique for the Powers hydraulic pressure theory are described in detail in Chapter 3.

Although the debate continues about Powers' theory, the critical spacing factor proposed in the hydraulic pressure mechanism is widely and successfully used to evaluate the freezing performance of concrete. Good results are confirmed by both laboratory and field work. However, when determining the spacing factor in Powers equation using the frequency and

specific surface area of air bubbles in a unit volume, the air bubbles are then assumed to have equal size and be distributed uniformly in a cubic lattice. Both assumptions are unrealistic, ignoring that spacing factor is affected by different air-bubble size distribution, different distributed locations or specific surface areas of air bubbles. Alternative spacing factors proposed by other researchers are also assumed to follow a Hertz distribution or Gamma distribution with parameters based on the mean diameter and the air-bubble specific surface area. Therefore, these spacing factors are not a physical property and they are constructed mathematically.

In order to evaluate the freezing and thawing performance of concrete accurately, new parameters of the air-void system of the hardened concrete are proposed in Chapter 4. By scanning and image processing for the concrete sections, the three-phase image can be obtained and aggregates, pastes and air voids are separated by different colors. The three-phase image makes it possible to determine the true spacing factor in the two-dimensional perspective. Every pixel of pastes in the image can be sought out and the distance from the paste pixel to its nearest air void can be calculated by Matlab. Then the average distance indicates the true spacing factor.

The volume of pastes within a distance from air voids in a unit volume of concrete can be protected during freezing. Based on stereology concepts and relationships, this volume of pastes can be determined by the area ratio of pastes on the section of polished concrete [23]. In addition, the air content in volume of hardened concrete can be determined by the area fraction of air voids on the scanning image of concrete sections. Both the percentage of protected pastes and the area fraction of air voids can be calculated based on the number of pixels of pastes and air voids on the resulting three-phase image. These calculations can be conducted by Matlab.

The surface area of air voids is significant to achieve the effective freezing and thawing resistance of concrete and it is a three-dimensional property. According to the relationship between the specific surface and boundary length on the sectional probes [24], the surface area of air voids in a unit volume of hardened concrete can be determined by the ratio of the perimeter of air voids on the section to the total area of the section. ImageJ can be used to calculate the perimeter of air voids from the three-phase image.

These two-dimensional parameters are proposed to evaluate the freezing and thawing performance of concrete considering the mechanism of freezing and the physical nature of concrete. Results of these parameters of the samples from CTLGroup and a comparison with the spacing factor, specific surface, and air content determined according to ASTM C457 are also shown in Chapter 4.

Chapter 2. Advances in Measuring Air-void Parameters in Hardened Concrete Using a Flatbed Scanner

This chapter presents improved techniques for acquiring images of the polished surface of hardened concrete using a flatbed scanner in order to measure the parameters of the air-void system. As a reference, the currently used ASTM C457 test will be discussed first.

2.1 ASTM C457 Test

Two test procedures are described in ASTM C457 standard including the linear traverse method and the point count method. Since the linear traverse method is also used in the scanning image analysis, its procedure will be discussed. The polished section of concrete is needed to provide the air-void system structure and operators observe the samples under a microscope. The sample is moved along straight lines and the linear distances traversed through air voids, aggregates, and pastes are measured. From the measured traversed length, the parameters of the air-void system can be calculated and shown below.

Air Content (A), in %:

$$A = \frac{T_a \times 100}{T_t} \tag{1}$$

Where T_a is the traverse length through air and T_t is total length of traverse.

Void Frequency (n):

$$n = \frac{N}{T_t} \tag{2}$$

Where N is the total number of air voids intersected.

Average Chord Length ($\bar{l}$):

$$\bar{l} = \frac{T_a}{N} \tag{3}$$

Or

$$\bar{l} = \frac{A}{100n} \tag{4}$$

Specific Surface (α):

$$\alpha = \frac{4}{\bar{l}} \tag{5}$$

Or

$$\alpha = \frac{4N}{T_a} \tag{6}$$

Paste Content (p), in %:

$$p = \frac{T_p \cdot 100}{T_t} \tag{7}$$

Paste-Air Ratio (p/A):

$$\frac{p}{A} = \frac{T_p}{T_a} \tag{8}$$

Spacing Factor ($\bar{L}$):

When p/A <= 4.342

$$\bar{L} = \frac{T_p}{4N} \tag{9}$$

When p/A > 4.342

$$\bar{L} = \frac{3}{\alpha}[1.4(1+\frac{p}{A})^{1/3} - 1] \tag{10}$$

In the image analysis, these parameters are also calculated according to the above equations. Since all the equations are statistically determined, the amount of sampling is significant. The traverse lengths are recommended by ASTM C457. With the large aggregate, the traverse length needs to increase.

2.2 Materials and Sample Preparation

In the experiment, six groups (labeled Group A to Group F) concrete samples provided by CTLGroup were analyzed. For group A, B, E, and F, each group had four thin sections with lengths larger than 50 mm. For Group C and D, each group had two thin sections for scanning. Since group C and D contained lightweight aggregates, it was difficult to analyze. A polishing machine, ASW-1800 was used in the polishing with high speed abrasion and water cooling. A wood frame was made with rollers to make the cylinder sections rotate freely. The samples were polished with three kinds of diamond disc with grits of 60, 260, and 800, respectively. The whole polishing took about 1 hour. After polishing with the 800-grit disc, a good smoothness of the surface required by ASTM C457 could be achieved. In addition, lacquer was sprayed on the surface of sections before polishing to protect the edge of air voids. Residue lacquer was removed by immersing the surface in acetone for 5 min after polishing. After drying the surface with an air flow gun, the surface was treated with a 1% phenolphthalein solution. The solution stayed for 1 min and rinsed with alcohol. After drying, the air voids of the surface were filled

with orange chalk powders with high brightness. The excess powders were removed using a blade scraping on the surface.

2.3 Image Analysis

The scanning was conducted with a Canon CanoScan 9000F flatbed scanner with the highest resolution of 4800 dpi or 5.3 μm per pixel. The maximum area of scanning was limited by 50×50 mm and each image was 255 MB. The scanning time is approximately 2 min. In the image processing, each pixel was identified as air voids, aggregates, or pastes and the scanning image was converted into a three-phase 8-bit image using Photoshop. Air voids in the image were displayed in white, aggregates in black, and pastes in gray. ImageJ was used to fill the holes in the aggregates in the creation of 8-bit image. When importing the 8-bit image into Matlab, the image was converted into a matrix with air voids represented by 255, aggregates by 0, and pastes by the number except 255 and 0. Automated calculation was conducted by Matlab for the parameters of the air-void system according to ASTM C457 and the results were exported into a spreadsheet. An illustration of scanning and three-phase image is presented in Figure 2.1.

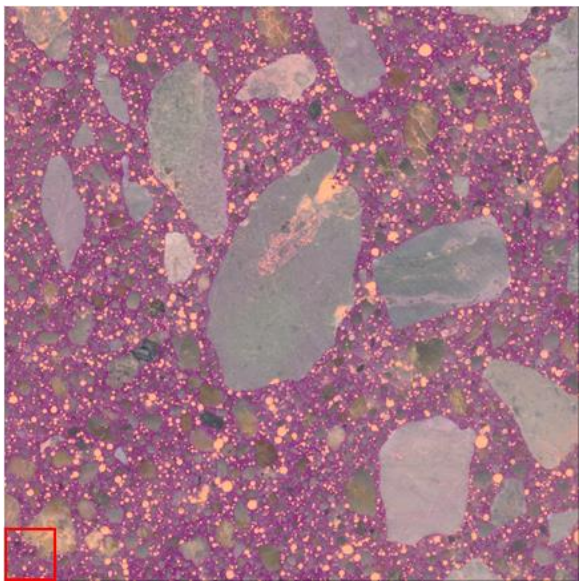

(a)

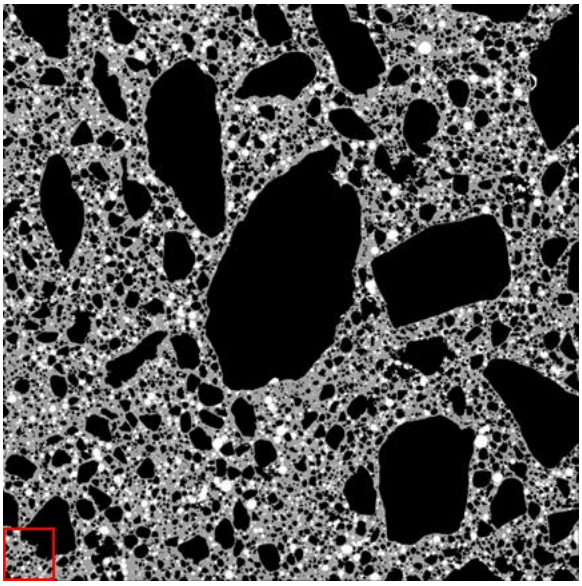

(b)

Figure 2.1: Original scanning (a);

Three-phase image (b).

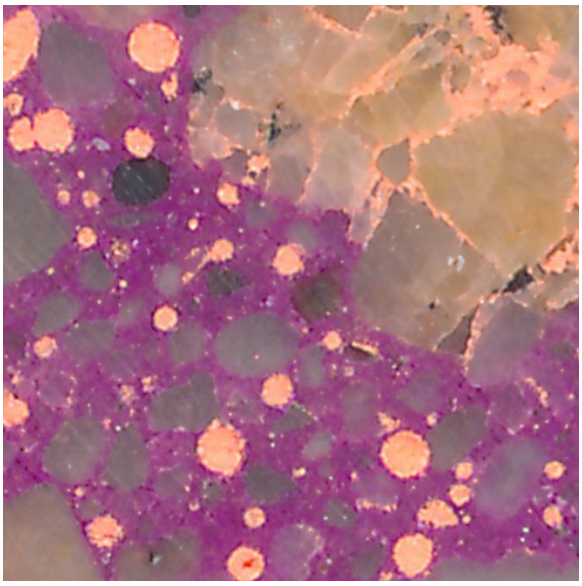

(c)

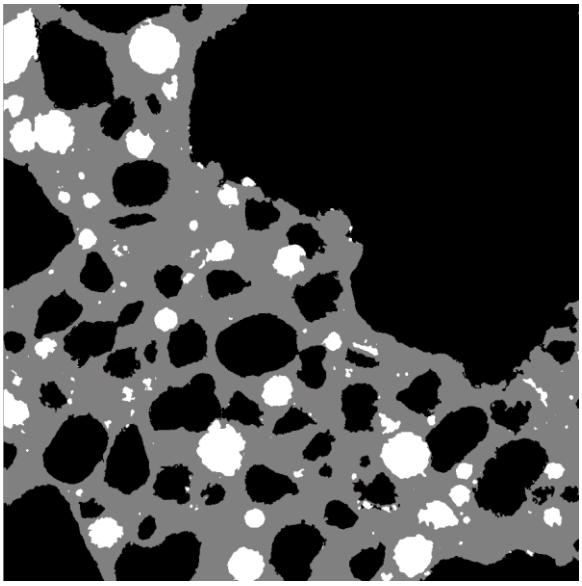

(d)

Figure 2.1 (cont.):

Magnification of the lower left corner of the original scanning (c);

Magnification of the lower left corner of the three-phase image (d).

The detailed polishing procedure and image processing are described in Appendix A. The original scanning images along with the three-phase images for all samples of Group A to F are shown in Appendix B.

2.4 Comparison with ASTM C457 Method

In this study, each section has been traversed 94 times along evenly distributed lines on the surface. In total, the traverse length for Group A, B, E, and F is 9250 mm and for Group C and D, 4625 mm, which are about four and two times larger than the minimum length required in ASTM C457, respectively.

The results of the calculated parameters and the reference provided by CTLGroup are shown in Table 2.1.

Table 2.1: Results of the calculated parameters and reference from CTLGroup.

Case	Paste [%]	Air [%]	Chord length [in]	Paste-air ratio	Specific surface [1/in]	Voids per inch	Spacing factor [in]
A1	31.37	6.87	0.0053	4.57	749.3	12.87	0.0059
A2	29.87	8.97	0.0060	3.33	664.0	14.89	0.0050
A3	34.72	8.19	0.0055	4.24	732.6	15.01	0.0058
A4	35.82	6.95	0.0060	5.15	665.0	11.56	0.0071
CTL-A	30.60	7.83	0.0082	3.90	487.0	9.53	0.0080
B1	29.75	6.56	0.0058	4.53	691.7	11.35	0.0064
B2	34.33	7.97	0.0061	4.31	651.3	12.98	0.0066
B3	41.59	7.20	0.0058	5.78	692.7	12.46	0.0071
B4	40.02	6.12	0.0057	6.54	698.1	10.67	0.0075
CTL-B	28.40	7.92	0.0071	3.59	566.9	11.22	0.0063
C1	28.07	13.75	0.0102	2.04	391.8	13.47	0.0052
C2	23.34	20.13	0.0124	1.30	352.8	16.70	0.0037
CTL-C	28.00	11.63	0.0081	2.40	494.6	14.39	0.0049
D1	45.75	36.38	0.0129	1.26	310.7	28.25	0.0040
D2	34.27	40.84	0.0136	0.84	295.0	30.12	0.0028
CTL-D	40.90	8.88	0.0059	4.60	674.4	14.97	0.0066
E1	28.25	6.57	0.0046	4.30	879.0	14.45	0.0049
E2	34.76	3.56	0.0037	9.76	1071.5	9.54	0.0059
E3	35.21	4.78	0.0039	7.36	1030.6	12.32	0.0054
E4	32.05	5.26	0.0048	6.09	839.9	11.04	0.0060
CTL-E	28.77	4.45	0.0045	6.46	881.0	9.80	0.0059
F1	21.84	6.22	0.0027	3.51	1462.2	22.74	0.0024
F2	29.38	8.88	0.0047	3.31	858.8	19.07	0.0039
F3	30.71	4.30	0.0037	7.14	1081.8	11.63	0.0050
F4	39.22	6.01	0.0038	6.53	1053.7	15.82	0.0050
CTL-F	24.69	5.22	0.0039	4.73	1022.5	13.33	0.0044

Comparison of the air content is presented in Figure 2.2. It can be seen that the difference is small between the calculated results and the reference from CTLGroup for Group A, B, E, and F. The differences are less than 1 percent. However, for Group C and D, the difference is much greater. For Group D, the calculated air content is even 4 time higher than the reference. These two groups of samples contain lightweight aggregate and there are many air voids in the aggregates. Therefore, it is difficult to distinguish the air voids incorporated in the pastes from those in the aggregates in the image processing and the significant difference is mainly caused by the difficult separation.

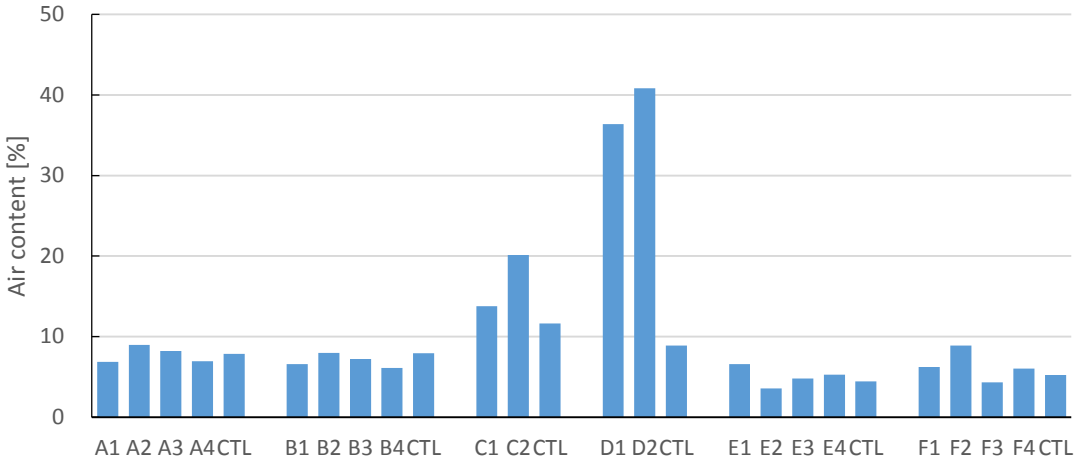

Figure 2.2: Comparison of the air content.

Specific surface and air frequency are interrelated and the mean size of the air bubbles can be reflected. The spacing factor is the average distance from the pastes to the edge of the nearest air void. Comparisons of the chord length, specific surface, and spacing factor are illustrated in Figure 2.3, 2.4, and 2.5. It can be seen that the calculated parameters have a good agreement with the reference results except those in Group C and D. The current technique for the automated measurement for the parameters is not applicable for the concrete with lightweight aggregates.

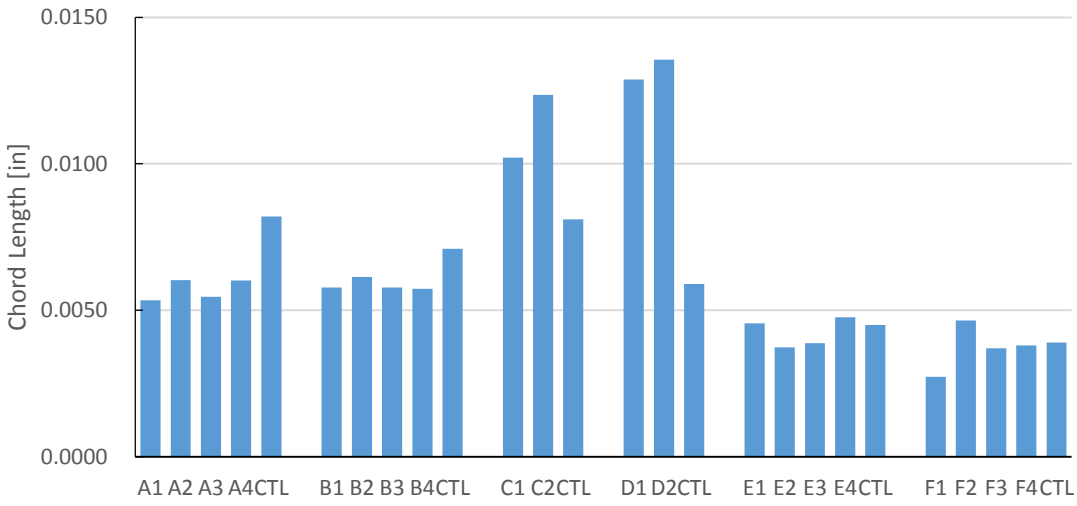

Figure 2.3: Comparison of the chord lengths.

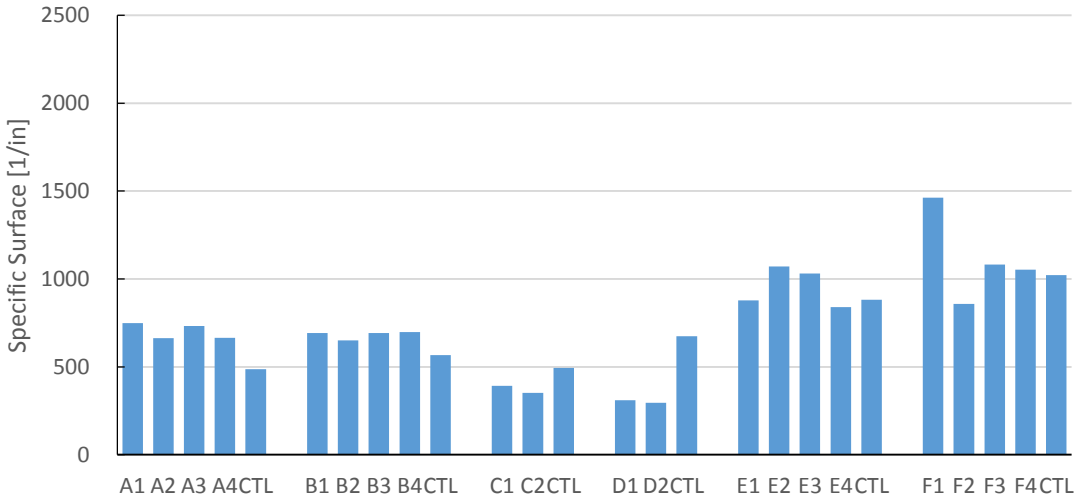

Figure 2.4: Comparison of the specific surfaces.

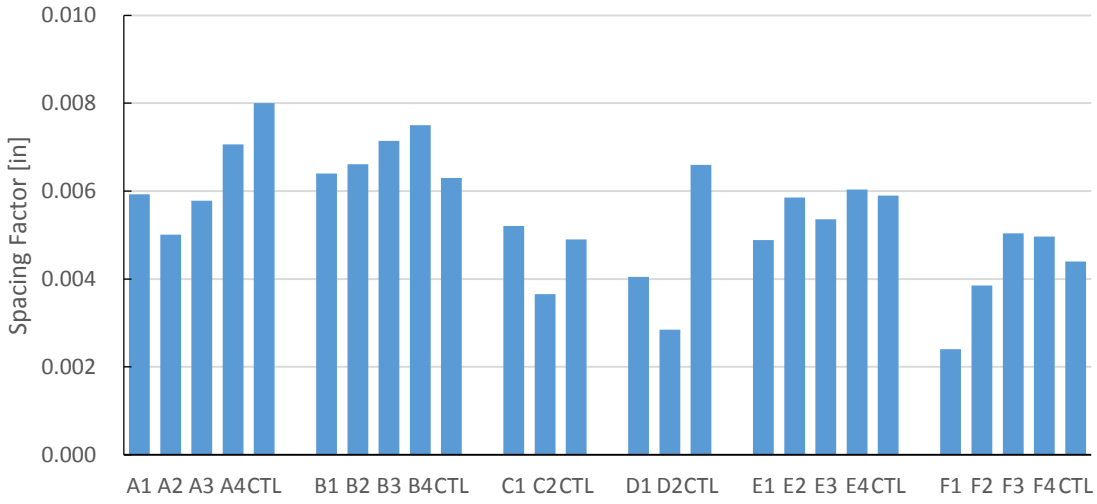

Figure 2.5: Comparison of the spacing factors.

2.5 Source of Error and Limitation in the Automated Measurement

All the parameters of the air-void system in hardened concrete are statistically based and the scanning area has an influence on the results. The maximum size of aggregates mainly controls the minimum size of the scanning area. With the larger aggregates, the traversed length through air and paste may decrease along with the number of air voids. To collect the same amount of sampling, the scanning area needs to increase. For Group E and F, the maximum size of aggregates is larger than other groups, and thus the air content varies more.

The air voids in the new method can be identified accurately, but the separation of the aggregates and the pastes needs to be improved. Figure 2.6 is an image from E1 magnified by 16 times. It can be seen from the three-phase image that the boundary of aggregates is not smooth but relatively fuzzy at a high resolution. Since the boundary of aggregates is easily to be stained by the phenolphthalein, the color in the boundary pixels is between the pink of pastes and the color of aggregates. Moreover, the automated measurement is based on the color of the pixels so that

the identification error is generated on the boundary of aggregates. In addition, the resolution of the scanner limits the boundary identification.

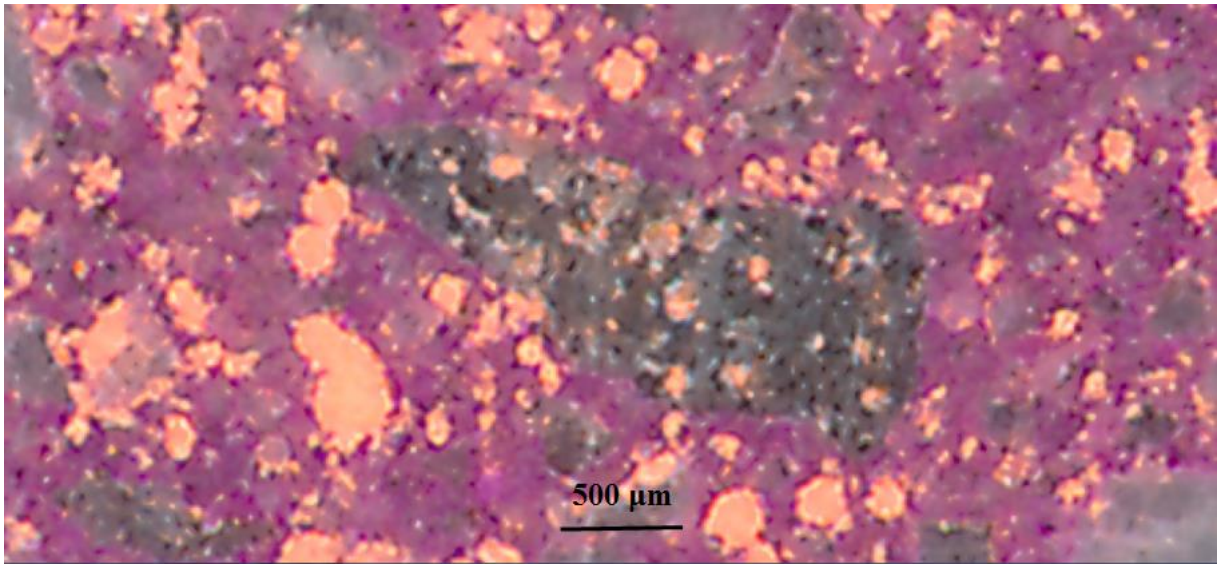

(a)

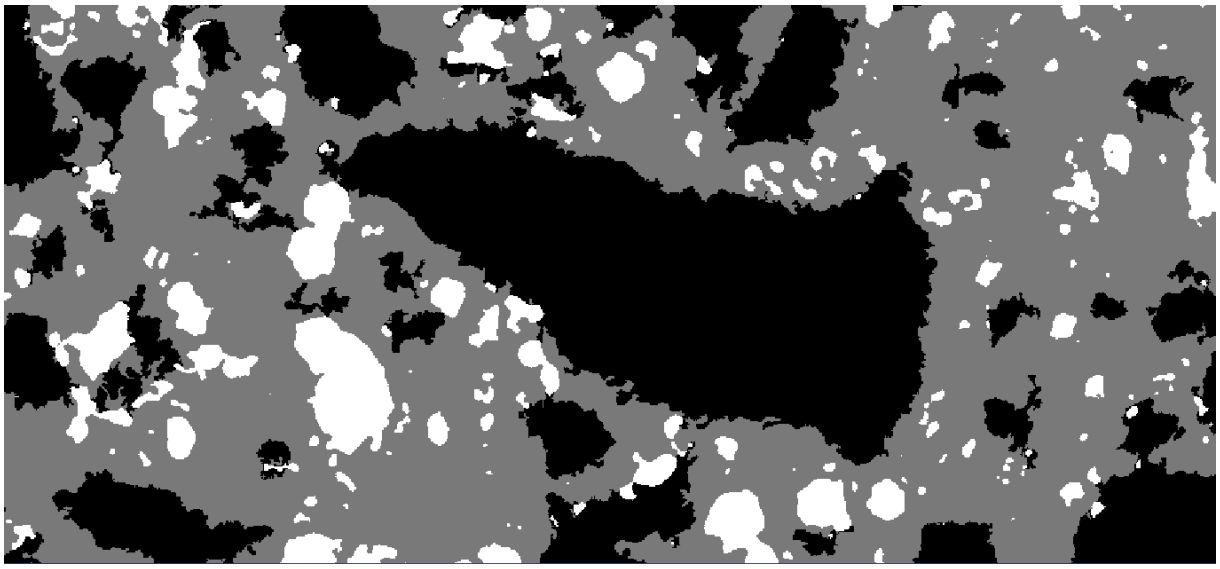

(b)

Figure 2.6: 16-time magnification of a sample (a); The three-phase image (b).

Sometimes, fine aggregates in concrete are partially transparent after polishing under high resolution so that these fine aggregates are difficult to identify. The fine aggregates can also be stained by the phenolphthalein and the variation of the color of the fine aggregates contributes to the difficulty in identification of fine aggregates.

Although these small errors exist in the image processing, parameters of the air-void system may not be influenced on a macro level. The localized errors of the identification do not usually make a difference in the parameters like air content since these parameters are statistically based and are determined by a large number of samples. The calculated parameters using flatbed scanners can provide reasonable results compared with the reference from CTLGroup.

Chapter 3. Mechanism of Freezing Action and Protective Function of Air Bubbles

When concrete is cooled below 0 ℃, most of the water in the paste will not freeze immediately. A wide spectrum of pore sizes exists, and water in capillary pores will freeze at the temperature below 0 ℃ by an amount that is dependent on the diameter of the pore due to thermodynamics. Even when the freezing temperature is reached, supercooled water can exist since a nucleus is required to initiate the formation of ice. Freezing point of water in different sizes of pores will be evaluated first.

The parameters of the air-void system in hardened concrete are expected to represent the physical nature during freezing so that it is necessary to revisit the mechanism of freezing. Many competing theories have been proposed in the last 60 years and they will be introduced in this chapter. Powers hydraulic pressure theory is the most referred theory and the critical spacing factor is employed to evaluate the freezing stress. However, there are criticisms for Powers' theory and it is necessary to determine whether it is appropriate to use the spacing factor as the parameter of the air-void system in hardened concrete.

3.1 Freezing Point of Water

Distilled water could become supercooling to -15 ℃ and maintained for several hours without a nucleation. In freezing concrete, water freezes with a seed, like an ice particle. However, the high curvature of the small pores in the concrete will greatly decrease the freezing point. The decrease could be estimated by the Gibbs-Thomson equation [25]:

$$\gamma_{CL}\kappa_{CL} = \int_{T}^{T_M(\infty)} \frac{(S_L - S_C)}{V_L} dT \tag{11}$$

Where γ_{CL} is the surface energy of ice-water interface, κ_{CL} is the curvature of the crystal in the pore, $T_M(\infty)$ is the freezing point of a macroscopic crystal, S_L and S_C are the entropies of the liquid and crystal, respectively, and V_L is the molar volume of the liquid.

When the entropies are assumed to be constant, the Gibbs-Thomson equation can be simplified to:

$$T = T_M(\infty) - \frac{\gamma_{CL}\kappa_{CL}}{(S_L - S_C)/V_L} \tag{12}$$

Where T is the freezing point of water in the pores and κ_{CL} can be calculated by the radius of the pore:

$$\kappa_{CL} = \frac{2}{r_{pore} - \delta} \tag{13}$$

Where δ is the thickness of the water layer which does not freeze between the crystal and the pore wall. For pure water, δ is about 0.8 to 1.0 nm, γ_{CL} is about 0.04 J/m^2, $(S_L - S_C)/V_L$ is about 1.2 J/(cm^3 K) [26]. Therefore, the freezing point of ice is -2 ℃ when r_{pore} is 33 nm, -5 ℃ when r_{pore} is 13 nm, -10 ℃ when r_{pore} is 7 nm. The freezing point of ice decreases with the decreasing pore radius, and thus water in the air voids with larger size will freeze first as the temperature drops.

3.2 Mechanism of Freezing Action

In order to improve the freezing and thawing performance of concrete, the mechanism of freezing action have been studied for a long time. There are a few theories to explain the source of freezing stresses, the reason for expansion during freezing, and ice formation. These theories will be discussed below.

3.2.1 Early Hypotheses

As water freezes, it expands by 9% of its original volume. It is believed that the resulting expansion in pores causes tensile strains in the pore wall. If the tensile strains exceed the capacity of the paste, cracking will occur and the concrete will fail eventually. However, this volume change is insufficient to account for all of the dilation observed in cement paste.

3.2.2 Hydraulic Pressure Theory

For many years, the major contribution to dilation was thought to be hydraulic pressure, which is proposed by T. C. Powers [16]. A series of equations were developed relating the spacing of air voids to the properties of the paste and the freezing rate. A simple mechanism settles the foundation of hydraulic pressure theory. When the temperature decreases below 0 ℃, water begins to freeze in the capillary pores and the volume increases. The formation of ice increases gradually due to the dissolved chemicals in the pores as the temperature decreases. If the capillary pores are saturated, a certain amount of water is forced out towards the available places without causing any damage, i.e. the air voids. Since the cement paste has a certain permeability, which water flow travels through, Darcy's law can be used to calculate the pressure required for water to travel a certain distance in a given time. If the pressure exceeds the tensile strength of the paste, the paste will crack in tension no matter because of the too long distance to travel or because of the too high freezing rate.

A single air bubble of radius r_b is surrounded by a shell of paste of thickness of L which is called the "sphere of influence of the bubble" in Figure 3.1. The maximum L_{max} of the shell refers to the maximum distance that water must travel through the paste and can be calculated in Equation 14. Above L_{max}, the hydraulic pressures generated by the water flow are sufficient to cause cracking of the paste.

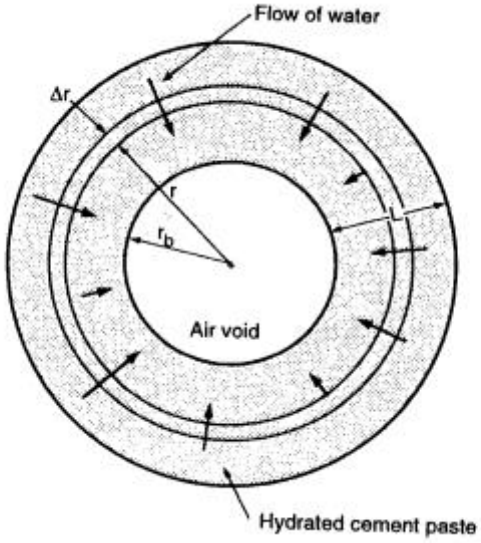

Figure 3.1: Air void surrounded by its sphere of influence of hardened cement paste [16].

$$\frac{L^3_{\max}}{r_b} + \frac{3L^3_{\max}}{2} = \frac{KT}{UR} \times (\text{constant}) \tag{14}$$

Where L is the thickness of the shell of the paste surrounding the air void, i.e. the thickness of the sphere of influence, r_b is the radius of the bubble, K is the permeability coefficient of the paste, T is the tensile strength of the paste, U is the quantity of water that freezes per degree of temperature drop, and R is the freezing rate.

Equation 14 assumes capillary pores are small compared to the size of air voids and are well distributed in the paste. It is shown that the maximum thickness of the sphere of influence around an air void decreases as the freezing rate increases, while it increases with the tensile strength and the permeability of the paste. If the water/cement ratio is high, the porosity and the amount of freezable water increases, and hence the maximum thickness needs to be reduced due to more water is forced out of the capillary pores. It is assumed that the amount of freezable water increases linearly with the decrease in temperature. Therefore, the minimum temperature that is

attained during freezing does not affect the phenomenon. Since only a single air bubble surrounded by a shell of paste is considered in the equation, it is theoretically applicable to pastes where all air voids are of the same size and are equally distributed. When the freezing rate is 11 ℃/h, the maximum value of $\bar{L}$ for a saturated paste is of the order of 250 μm.

The average value of the maximum distance that water must travel to reach an air void could be estimated by the average half-distance between two adjacent air-void walls for all air voids in the paste and it is called spacing factor, $\bar{L}$. This method is adopted by the American Society for Testing and Materials (ASTM) and is described in ASTM C 457: Microscopical Determination of Air Void Content and Parameters of the Air Void System in Hardened Concrete [2]. Other air void spacing factors will be discussed below.

The hydraulic pressure theory can explain the test results on the influence of the freezing rate and it is the only one to establish mathematical relationships between the freezing rate, the paste properties, and the spacing factor. However, the basic mechanism seems incorrect since numerous experiments have shown the water tends to travel to and not from air voids when it freezes. Even if the basic mechanism seems to be incorrect, it takes into account the most relevant parameters regarding resistance to freezing and thawing cycles, the spacing of air voids. To avoid frost damage to the paste, water needs to move to the air voids to freeze and air voids must be sufficiently close to offer the adequate protection.

3.2.3 Energy of Solidification Theory

As discussed above, larger pores can freeze at higher temperatures than smaller pores so that at a given temperature below 0 ℃, ice can only form in some larger pores. The unfrozen water in smaller pores is in a supercooled state. Based on thermodynamics, the ice in the larger pores is at a low-energy state, and the supercooled water in the small pores is at a high-energy state since

the water contains some latent heat of fusion. According to the Gibbs equation, the molar Gibbs free energy of water is higher than that of ice. Therefore, a driving force impels the supercooled water to travel to the site of freezing where it can freeze and release its latent heat of fusion [17]. D.H. Everett and J.M. Haynes [27] showed that ice in the larger pores would grow to the smaller pores filled with water when a curved connecting tube exists between the larger and smaller pores. A pressure would be induced in the smaller, unfrozen pore water due to the curvature and would draw water to the ice crystal until ice could not expand further because of lack of space.

A tendency is indicated that water actually flows towards the freezing site, instead of away from it as described by the hydraulic pressure theory. However, the hydraulic pressure theory has not been invalidated inevitably. As freezing occurs in a large pore, supercooled water in the surrounding small pores tends to travel to the large pore due to thermodynamics. When the large pore is filled with ice and no further space exists, the hydraulic pressure will be prominent in the mechanism.

3.2.4 Osmotic Pressure Theory

When Powers and Helmuth discovered the fact that water tends to move towards the capillary pores where ice is forming and shrinkage in the paste occurs, they suggested a new hypothesis to explain the action of freezing [18]. If the temperature decreases below 0 ℃, water does not freeze immediately. It is because the dissolved chemicals (mainly the alkalies Na_2O and K_2O) reduce the temperature of the ice formation and so does surface tension of water in the relatively small size of pores. When the temperature drops, water begins to freeze and the concentration of dissolved chemicals increases until the melting point of the solution becomes equal to the value of the temperature. Since the concentration in the small pores is smaller than that in the larger pores where ice forms, water in the small pores is attracted to the larger pores due to osmotic

phenomenon, which is shown in Figure 3.2. Therefore, internal pressures start building up once ice forms if the paste is saturated and the osmotic pressure due to the movement of water increases the internal stresses in the paste. As water arrives in the pore where the ice has formed, more ice can form due to the decreasing concentration of the solution.

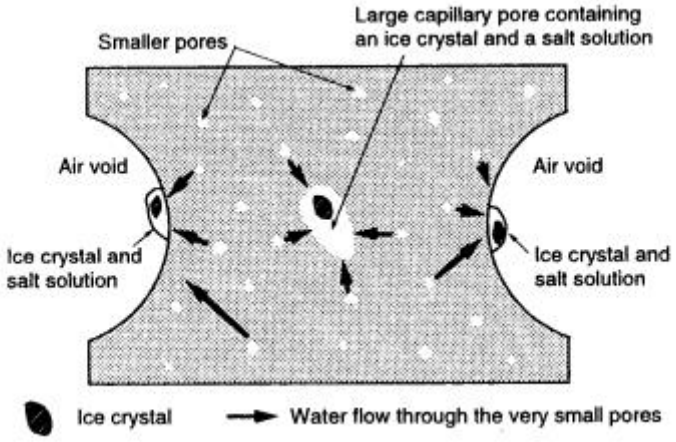

Figure 3.2: Schematic illustration of the osmotic pressure theory [28].

Air voids could compete with the capillary pores where ice is forming to attract water. They normally contain a little water and ice can therefore form on the walls of the air voids. If the air voids are sufficiently closely spaced, the paste is then protected from freezing damage.

This model can explain many experiments results, for example, the shrinkage during the freezing. It can also explain the effects of de-icer salts which increase the osmotic pressure phenomenon. However, the influence of the freezing rate cannot be explained. According to this theory, the length of the freezing period and not the freezing rate is important because long freezing periods promote ice-crystal growth.

3.2.5 Litvan's Theory

Litvan proposes that the water in the capillary pores cannot freeze in situ when the temperature of the paste decreases below 0 ℃ and is thus supercooled [19]. The supercooled water can cause drying of the paste because the vapor pressure over supercooled water is higher than that over ice. In frost action of hardened cement paste, a non-equilibrium situation creates until the vapor pressure of supercooled water in the capillary pores decreases sufficiently and has reached the value corresponding to that of ice. When the freezing rate is too high, or the distance that water must travel to reach an external surface and freeze is too long, the process of desorption, i.e. moisture transfer, cannot occur in an orderly manner. Thus, mechanical damage occurs. In the freezing process, the very rapid drying process forces the movement of water. Therefore, the high stresses and cracking are caused.

Litvan's theory is compatible with observations in the freezing process, such as the effects of freezing rate, the role of entrained air, and the influence of de-icer salts. The higher the freezing rate, the larger the amount of unstable water and the more severe mechanical damage. Entrained air decreases the distance that water must travel by providing space where water can freeze. Litvan concluded that the de-icer salts in the pore water solution decrease the vapor pressure and hinder the possible drying in the freezing and thawing. It also increases the difference between the vapor pressure over the supercooled water in the capillary pores and that over the ice formed on external walls of the paste and thus amplifies the phenomenon causing the flow of water through the paste. It explains the fundamental phenomenon, the forced movement of water due to the vapor pressure difference. However, it cannot establish a clear relationship between the spacing of air voids, the freezing rate and the paste properties.

There seem to be many contradictions between these theories, but they are often more apparent than real. In many respects, these theories complement each other and each of them really explains only certain parts of the overall phenomenon.

3.2.6 Chatterji's Theory

S. Chatterji [20] expanded the ice penetration model to explain the freezing action of air-entrained cement materials. In the freezing, water in the paste expands from 4 ℃ to 0 ℃ and some water will be pressed into air bubbles. Besides, the pressure in the air bubbles will drop during cooling, water will be drawn in. Then, a layer of water will form on the surface of the air bubbles. Due to the surface tension, the water will spread as annular layers in the air bubbles. Air-entraining admixtures make hydrophobic layers precipitating on the surface of air bubbles. When ice forming, dendritic ice penetrates the concrete, the ice reaches the air bubbles, and the annular water layer on the surface of air bubbles freezes into the ice layer. The thin precipitated hydrophobic layer then separates the ice layer and the cement pastes. On further freezing, whether the annular ice layer grows in the air bubbles or develops further dendritic penetration depends on the Laplace- Dupree equation [29].

$$\Delta p_i + \Delta p_w = \frac{2\gamma_{iw}}{r_i} \tag{15}$$

Where Δp_i is the restraining pressure acting on the ice crystal and is mainly the ice-substrate bonding, Δp_w is the suction pressure in water, γ_{iw} is the ice-water interfacial tension, and r_i is the radius of the capillary pores or gel pores.

To avoid that ice penetrates into the cement pastes, Δp_i needs to be lower than a critical Δp_i for a given r_i. The ice-substrate bonding depends on the nature of the surface of the substrate and when the ice layer contacts with the hydrophobic layer of the air-entraining admixtures, the ice-

substrate bonding decreases with the degree of hydrophobicity. Therefore, Δp_i will be affected by the type of air-entraining admixtures. When Δp_i is low enough, the annular ice layer will grow into the air bubbles and water in the surrounding capillary pores will be drawn towards the ice layer. The suction of water will not cause damage to the cement paste since the resulting hydraulic pressure is under the atmospheric pressure. In this way, the cement paste is protected by the water transfer caused by the air bubbles.

With the growth of the ice layer, the air pressure will be raised due to the progressive air compression and will stop the further growth of the ice layer if the air pressure is high enough. Afterwards, dendritic ice penetration occurs in the cement paste, which will increase the hydrostatic pressure of the unfrozen water. The developed hydrostatic pressure could cause damage to the paste with sufficient volume of unfrozen water.

3.2.7 Crystallization Pressure Theory

Crystallization pressure is utilized to explain the internal stresses and cracking by G. W. Scherer [21]. Crystallization pressure is produced by disjoining pressure between the minerals in the pore surface and the ice crystal. Since the ice phase has a lower refractive index and lower density than the water phase, the refractive index of water lies between the ice and the mineral at their interface so that the van der Waals forces are repulsive between the ice and the mineral. Besides, electrostatic forces and the structuring of the solvent contribute to the disjoining pressure at the solid surface. When the ice crystal forms in pores, a water film always exists between the ice and the pore wall. Therefore, the pore wall will be exerted by the pressure due to the equilibrium of the water film as ice grows in air voids. The magnitude of the crystallization pressure is shown as below:

$$P_A = \gamma_{CL}(\kappa_{CL}^{E} - \kappa_{CL}^{S}) \tag{16}$$

Where κ^{E}_{CL} and κ^{S}_{CL} are curvatures of crystal at the pore end and pore side, respectively, γ_{CL} is the surface energy of the ice-water interface.

For a cylindrical pore, the curvature of crystal at the pore side is equal about half of the curvature of crystal at the pore end and the crystallization pressure can be expressed as:

$$P_A = \gamma_{CL}(\kappa_{CL}^{E} - \frac{1}{2}\kappa_{CL}^{E}) = \frac{1}{2}\gamma_{CL}\kappa_{CL}^{E} = \frac{\gamma_{CL}}{r_{pore} - \delta} \tag{17}$$

Where δ is the thickness of the water layer between the ice crystal and the pore wall.

From the equation, the crystallization pressure increases with the decreasing pore size and it will yield the tensile strength of the concrete for small pore size.

3.2.8 Cryo-suction Theory

Coussy and Monteiro [22] combine the hydraulic pressure and the cryo-suction process to interpret the freezing mechanism of concrete and apply the unsaturated poroelasticity theory to compute stresses and strains developed based on the complex mechanism. On the one hand, when some water in the pores freeze, the hydraulic pressure will build up and expel the unfrozen water to flow from the freezing sites to other pores network. On the other hand, cryo-suction effects draw water from the capillary pores to the freezing sites on the further cooling. Poroelasticity and continuum thermodynamics help to determine the deformation in concrete during the phase transformation of the water inside the porous and deformable concrete. The hydraulic pressure and cryo-suction effects are considered in the model of freezing concrete. In the poroelasticity equations, the effect of pore size distribution is evaluated on the intensity of strain in concrete and on the build-up pressure on the cement paste. Air voids then have two

effects: they are both expansion reservoirs and efficient cryo-pumps. Their respective effects can be assessed quantitatively in this theory.

3.3 Evaluation of Powers Hydraulic Pressure Theory

Helmuth evaluated assumptions of Powers hydraulic pressure theory and found some invalid conclusion. For example, he found that air bubbles are not empty. It is about 36% that are filled with water in the entrained air voids of the virgin pastes within 24 h [30]. Water spreads on the surface of the air voids as an annular layer due to the surface tension. Powers assumed that ice nucleation is homogeneous so that the initial nucleation will occur in the annular layer without the size restriction in capillary pores. However, these annular layers on the surface of air voids will freeze with the temperature dropping and they will block water in the capillary pores flowing into the air voids. In another paper [31], Helmuth demonstrated that dendritic ice penetrates into air voids instead of homogeneous nucleation in the concrete. Efficient ice paste bonding and supercooling of water could aggravate the dendritic ice penetration [29].

In addition, Powers predicted based on his equation that the expansion of concrete will increase with the increasing rate of freezing. However, Helmuth showed that the increasing rate of freezing actually decreases the expansion [32]. Chatterji [20] explained the decreasing expansion using some contributory factors including a water transfer from capillary pores to gel pores when lowering the temperature, outer volume of the concrete filling with ice, and increasing strength due to the ice filling. Ice will contract at sub-zero temperature and the concrete will be compressed. Therefore, the compression reduces the possible expansion.

Thirdly, Powers supposed that capillary or gel pores need to be saturated to generate hydraulic pressure to damage the paste. However, Helmuth found that freezing damage may occur in self-desiccated paste having unsaturated capillary or gel pores [32].

Another issue that cannot be explained by the Powers hydraulic pressure theory is that different air-entraining admixtures have different degrees of improvement in the freezing and thawing resistance of the air-entrained concrete. Mielenz [33] evaluated the freezing and thawing performance of concrete samples using different air-entraining admixtures but with similar composition and volume of entrained air. To eliminate the effects of different spacing factors and air-bubble size distributions in different concrete samples, Chatterji [34] used one single batch of industrial aerated product hydrothermally to obtain cylindrical samples with different air-entraining admixtures. Since the material and air voids characteristics are kept the same and the only variable is the air-entraining admixtures, the freezing and thawing resistance is shown to depend on the chemical nature of the air-entraining admixtures. Furthermore, in ASTM C233 and ASTM C260 [35, 36], all air-entraining admixtures are required to compare with vinsol resin in freezing and thawing performance, which indicates that the air-entraining admixtures have their specific effects and the effects are not equal.

Besides, Monteiro et al. [37] showed that the paste was considered as a rigid body in Powers' model so that the mechanical response of the porous and deformable material cannot be predicted considering the complex interaction between air voids and water flow.

Chapter 4. New 2D Parameters of the Air-void System in Hardened Concrete

Although discussion and debate continue about Powers' model and hydraulic pressure theory, the critical spacing factor proposed in the hydraulic pressure model is successful to evaluate the freezing and thawing resistance, which is confirmed in both laboratory and field work. Chatterji explained [20] the success of spacing factor. When the dendritic ice penetrates into the air voids during freezing, the annular water layer on the surface will freeze. For the given air-entraining admixtures, the thickness of the water layer or the later ice layer is fixed. Since the ice layer stops the further water flow into air bubbles, the maximum amount of water drawn from the paste is proportional to the surface area of the air bubbles. If more water is drawn from the paste into air bubbles, the freezing and thawing performance of concrete is better. Since spacing factor is inversely related to the surface area of the whole entrained air system, the lower spacing factor indicates a higher surface area of the air bubble system and better concrete freezing resistance. A number of equations including Powers equation are used to characterize spacing factor of the air void system in air-entrained concrete, which will be discussed below.

Global microstructural parameters including volume, surface area, and object number are useful in some experimental studies. Three-dimensional parameters are not apparent while two-dimensional images or sections of a sample can provide visualized information so that the two-dimensional parameters can be analyzed accurately. However, these two-dimensional images lost some information and the obtained parameters may deviate from the true properties. Solids in turn into areas in two dimension, surfaces into lines, and lines into points. Therefore, the relationship between two-dimensional and three-dimensional parameters of a sample has to be learned. Stereology, as a set of mathematical methods, infers global microstructural parameters and three-dimensional geometry of samples based on measurements collected from two-

dimensional images or sections [38]. Usually, the actual determination of the three-dimensional parameters is not necessary and hence estimation with statistical margins of error is appropriate in most cases. With the increasing number of samples, the error will be controlled. In the sampling, the critical factors include representative samples and orientation of the samples.

The ratio of the area of the sectional profile of objects to the total area of the section is represented by A_A, the ratio of the length of the sectional profile of objects lied over by linear probes to the total length of the probes presented by L_L, the ratio of the number of points interacted with the profile of objects to the total number of points on the section presented by P_p, and the ratio of the volume of embedded objects to the total volume of the sample presented by V_V. Delesse proved that VV=AA in 1847 [39], Rosiwal demonstrated that VV=LL [40], and VV=PP is proved in 1930 [41]. These relationships can be illustrated in Figure 4.1. As the number of samples is increasing, the average of the ratios will reach the true values.

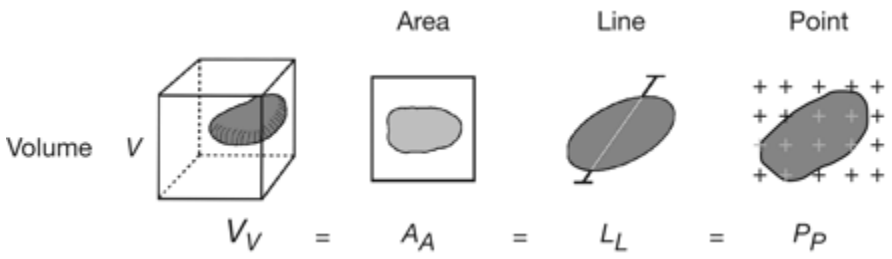

Figure 4.1: Mathematical relationship between different interaction probes [23].

A series of new two-dimensional parameters are proposed based on stereology concepts and relationships, such as the average distance of pastes to the nearest air void, the percentage of protected pastes, the area fraction of air voids, and the surface area of air voids. A comparison between these parameters and the reference parameters in ASTM C457 is conducted in this chapter.

4.1 The Entrained Air-void System and Spacing Factor

Entrained air is distributed in the paste as fine bubbles and the structure of the air-void system is critical to guarantee the frost resistance. The spacing factor is one of the most critical parameters of a satisfactory air void system, which is defined as the average distance from any point in the paste to the edge of the nearest void to ensure adequate freezing protection. The air void spacing equations have been proposed by a number of researchers: Powers, Philleo, Attiogbe, and Pleau and Pigeon. The true spacing is attempted to be characterized by these spacing equations.

The structure of the air-void system is essential to obtain satisfactory frost resistance. Tiny bubbles entrained are dispersed throughout the paste with an approximately spherical shape and diameter from 0.05 mm to 1.25 mm [1]. The critical parameters of a satisfactory air-void system are the spacing factor, specific surface area, and bubble frequency according to ASTM C 457. The specific surface area and bubble frequency are interrelated and used to reflect the mean size of the bubbles while the spacing factor which is introduced above is the average distance from any point in the paste to the edge of the nearest void. The spacing factor is the most commonly used parameter to ensure adequate freezing-thawing protection. A well-distributed system of small bubbles could protect the entire paste volume and quantitative microscopic examination can be conducted to determine these parameters using automated computer-based systems.

With the same air content, it could be expected that different air void spacing should exhibit different freezing-thawing performance. Therefore, an air-void system could be characterized by estimating some measure of air void spacing. A number of equations attempts to characterize the air void spacing in air-entrained concrete, which will be discussed below.

For nomenclature for air void quantities in different equations, a set of common notation is used to express quantities and given below:

n: number of air voids per volume

A: air void volume fraction

p: paste volume fraction

α: specific surface area of spheres

r: sphere radii

f(r): sphere radii probability density function

$\langle R^k \rangle$: the expected value of R^k for the radius distribution

s: spacing distribution parameter.

Quantities of the paste-air systems can be defined in Equations 18-21:

$$A \equiv \frac{4\pi}{3} n \left\langle R^3 \right\rangle \tag{18}$$

$$p \equiv 1\text{-}A \tag{19}$$

$$\alpha \equiv \frac{4\pi n \left\langle R^2 \right\rangle}{\frac{4\pi n}{3} \left\langle R^3 \right\rangle} \tag{20}$$

$$\left\langle R^k \right\rangle \equiv \int_0^\infty r^k f(r) dr \tag{21}$$

4.1.1 Powers Spacing Factor

The most widely used spacing factor equation is the Powers spacing factor [16]. The air voids are entrapped or entrained into the paste and some fraction of the paste could be protected by these air voids within some distance. The distance of the paste from the surface of the air bubbles

is estimated, but the value of the paste fraction cannot be quantified. To develop the Power spacing factor, two idealized systems are employed. If the p/A ratio is small, all of the paste is assumed to spread into a uniformly thick layer over every air void when. If the p/A ratio is relatively large, the cubic lattice approach is used and all air voids are supposed to have the same size. Therefore, the resulting spacing factor can be estimated using the distance from the center of the cubic cell to the nearest air void surface. The equations are shown below.

$$\bar{L} = \frac{p}{4\pi n\left\langle R^2 \right\rangle} = \frac{p}{\alpha A} \cdots p / A < 4.342 \tag{22}$$

$$\bar{L} = \frac{3}{\alpha}\left[1.4\left(\frac{p}{A}+1\right)^{1/3} - 1\right] \cdots p / A \geq 4.342 \tag{23}$$

When the p/A equals 4.342, these two equations will have the same value of the spacing factor.

4.1.2 Philleo Spacing Equation

Philleo extended the Powers' approach by quantifying the volume fraction of the paste within a distance from an air void [42]. Philleo spacing equation has an ideal air void system with randomly distributed points with known statistics and then modified to account for finite-sized spheres. The result characterizes the spacing of the paste to the finite-sized air voids. For a paste-void system, the Philleo spacing factor estimates the volume fraction of paste within a distance s from an air void surface [42]:

$$F(s) = 1 - \exp[-4.19\,\mathrm{x}^3 - 7.80\,\mathrm{x}^2[\ln(1/p)^{1/3} - 4.84x[\ln(1/p)]^{2/3}] \tag{24}$$

Where the substitution $x=sn^{1/3}$ has been made.

4.1.3 Attiogbe Spacing Equation

Attiogbe [43] proposed a spacing equation to estimate the mean spacing of air voids in concrete. In this equation, geometric probability concepts and stereological principles are used to derive the mean spacing of air voids.

$$t = 2\frac{p^2}{\alpha A} \tag{25}$$

By a numerical test, Attiogbe suggested that the equation is valid for all values of paste-to-air ratio, p/A and the mean spacing yields a better estimate of the actual spacing of the air voids in hardened concrete than the Powers spacing factor.

4.1.4 Mean Free Path

The mean free path is calculated by the average chord lengths in the paste, which is determined by Equation 26 [44]:

$$\lambda = \frac{p}{n\pi\left\langle R^2\right\rangle} \tag{26}$$

If the centers of the air voids are fixed, as the radii of these air voids are decreasing to zero, the mean free path changes to infinity, which equals to t in the Attiogbe equation. In fact, t in the Attiogbe equation is directly proportional to λ [44]. The Attiogbe equation t can be expressed as:

$$t = 2p\frac{p}{\alpha A} = \frac{p}{2}\frac{p}{n\pi\left\langle R^2\right\rangle} = \frac{p}{2}\lambda \tag{27}$$

Therefore, t in the Attiogbe equation approximately equals to half of the mean free path in a paste-void system.

4.1.5 Pleau and Pigeon Spacing Equation

Pleau and Pigeon proposed a spacing equation for the spacing distribution of the paste-void system [45]. Both the radii distribution of the air voids and the distribution of the distance from a random paste particle to the center of the nearest air void are considered. h(x) represents the PDF of the distance from the random particle in the paste to the center of the nearest air void. For an approximation, h(x) can be expressed as:

$$h(x) = 4\pi n e^{-(4/3)\pi n x^3} \tag{28}$$

By integrating a joint probability over the possible radii where s is the distance from the random particle to the surface of the nearest air void with radius r, the probability is determined as:

$$k(s) = \int_0^\infty h(r+s)\, f(r)\Theta(r+s)dr \tag{29}$$

Where the Heaviside function $\Theta(r+s)$ ensures that the function h keeps positive. The CDF corresponds to the volume fraction of the paste system within the distance s of an air void surface, which is:

$$\mathrm{K}(s) = \frac{1}{Q}\int_0^s k(s')ds' \tag{30}$$

Where Q is used to normalize the result by the volume fraction of the paste, which equals 1-A.

4.2 Average Distance of Pastes to the Nearest Air Void

Since the above spacing factors proposed by Powers and other researchers are not a physical property, the freezing and thawing resistance cannot be evaluated in a straightforward and accurate way. The distance from water in the capillary pores or gel pores of the paste to the

nearest air void is of importance to indicate the true spacing factor. This distance in fact represents how far the water needs to travel to air voids.

Based on the novel method to determine the parameters using flatbed scanners, the three-phase image of concrete sections can be obtained. All pastes pixels can be displayed in gray color in the image. Therefore, the distance of pastes axils to the nearest air void could be used to determine the distance of water in capillary pores or gel pores to the nearest air void. The air void pixels are displayed in white color in the three-phase image. Matlab can be used in this calculating process since the three-phase image can be easily imported in the Matlab and converted into matrix. For a grayscale image, black pixels are converted into 0, white pixels into 255, and gray pixels into the rest number in the matrix. In this situation, aggregates are converted into 0, air voids into 255, and pastes into the rest number in the matrix. If the matrix of the three-phase image is obtained, a large enough area is given from each pastes pixel. Within the area, the distances from the paste pixel to all air voids pixels are calculated and the minimum distance is then recorded. All minimum distances of all pastes pixels are averaged to characterize the spacing factor. However, in the scanning image, about 1 million $\times$ 1 million pixels are collected and about 20 million pixels are cement pastes. If all minimum distances of all these pastes pixels are exported and saved, a large number of data are not easy to manage. More importantly, there is no need to analyze all the distances since the distribution and the average value of the distances are what we concern. Therefore, the whole scanning image along with the three-phase image of concrete sections is divided into 50$\times$50 parts and the average minimum distance of pastes pixels in each part is exported. The distribution of average distance of these 2500 parts indicates the distribution of all distance of pastes pixels in the three-phase image and the average of the 2500 distances indicates the average of all pastes pixels. In Table 4.1, the error of the

estimation is shown for the average distance of the 2500 parts. Table 4.1 indicates that the largest error is less than 8% and most of the errors are below 5%. The samples from CTLGroup are analyzed to determine the new spacing factor and the results will be introduced in the following part.

Table 4.1: Error of the estimation for the average distance of the 2500 parts.

Sample	Average distance (μm)		Error
	Average of all pastes	Average of 1500 parts	
A1	150.53	157.5985	4.70%
A2	118.03	127.2189	7.78%
A3	122.15	122.7995	0.53%
A4	125.26	130.4589	4.15%
B1	126.13	133.0157	5.46%
B2	142.14	150.0286	5.55%
B3	112.35	116.6622	3.84%
B4	135.72	140.4461	3.49%
E1	95.99	96.3043	0.33%
E2	129.72	130.8897	0.90%
E3	101.38	99.9617	1.40%
E4	111.42	111.2188	0.18%
F1	81.72	76.3690	6.55%
F2	71.61	68.1956	4.77%
F3	95.98	95.5768	0.42%
F4	86.68	85.0778	1.85%

For sample E3, the cumulative relative frequency of the average distance in the 2500 parts is shown in Figure 4.2. It can be seen that 90% of average distances are below 140 μm and 50% below about 90 μm. The average distance of E3 is calculated and equals to 101.38 μm. Although the value of the spacing factor is small enough for a good freezing and thawing resistance, there

are some areas whose average distance of pastes pixels to the nearest air voids exceeds 200 μm or even 250 μm.

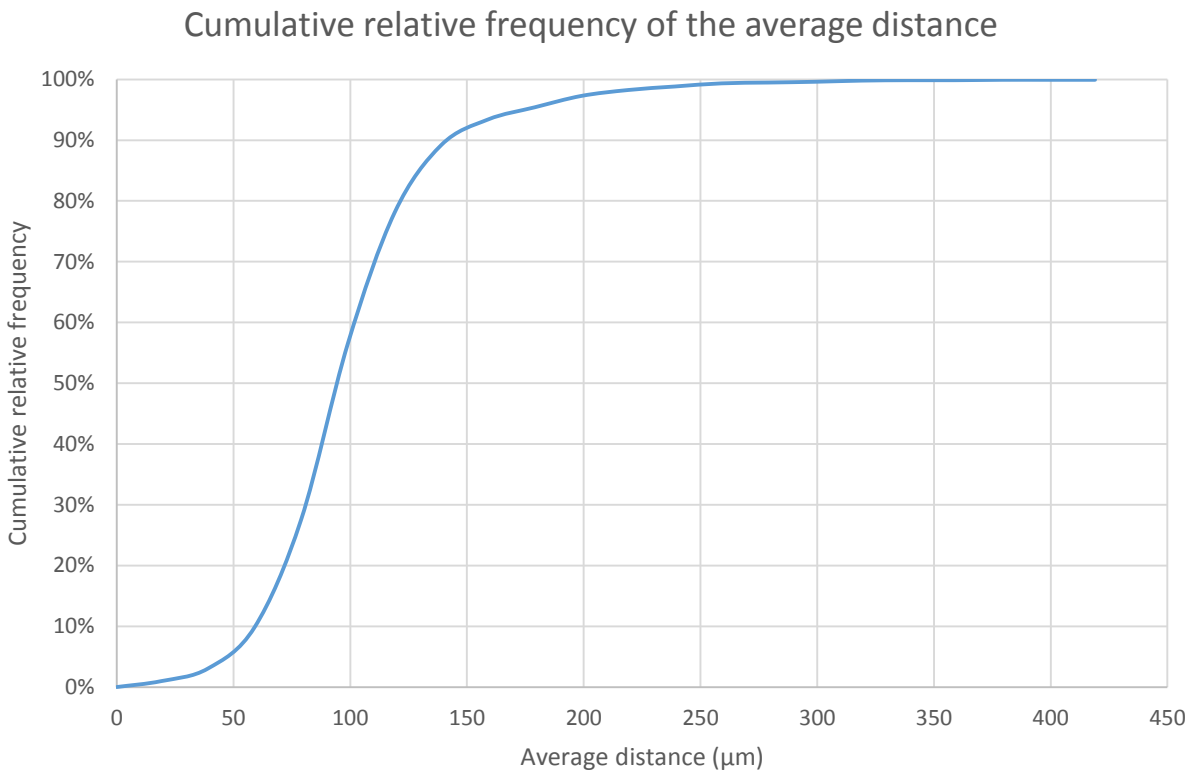

Figure 4.2: Cumulative relative frequency of the average distance of E3.

Another advantage of the method that the three-phase image is divided into 50×50 parts and analyzed using Matlab is that the areas with larger average distances can be picked out. In Figure 4.3, the red areas have the average distance greater than 250 μm. For sample E3, the easily damaged areas are on the edge of some coarse aggregates. Most of some red areas, for example the two areas on the lower right corner, locate on coarse aggregates, but some pastes pixels can be seen when the image is zoomed in. Since no air voids in coarse aggregates or no passing channel to coarse aggregates is assumed, the water in the pastes on the edge of coarse aggregates

can only flow towards other directions. Therefore, some easily damaged areas may be on the edge of coarse aggregates.

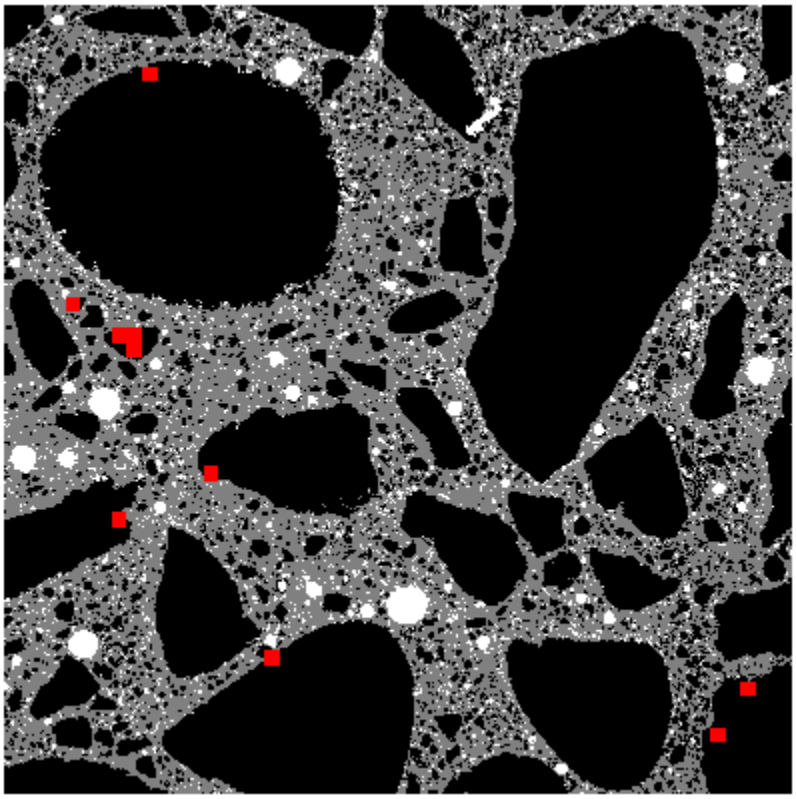

Figure 4.3: Easily damaged areas of E3.

For sample B4, the cumulative relative frequency of the average distance can be shown in Figure 4.4. It can be seen that 90% of average distances are below 220 μm and 50% below about 125 μm. The average distance of E3 equals to 135.72 μm. Compared with sample E3, the average distance of sample B4 is larger and more areas in sample B4 have the average distance more than 250 μm. The easily damaged areas of B4 are shown in red in Figure 4.5.

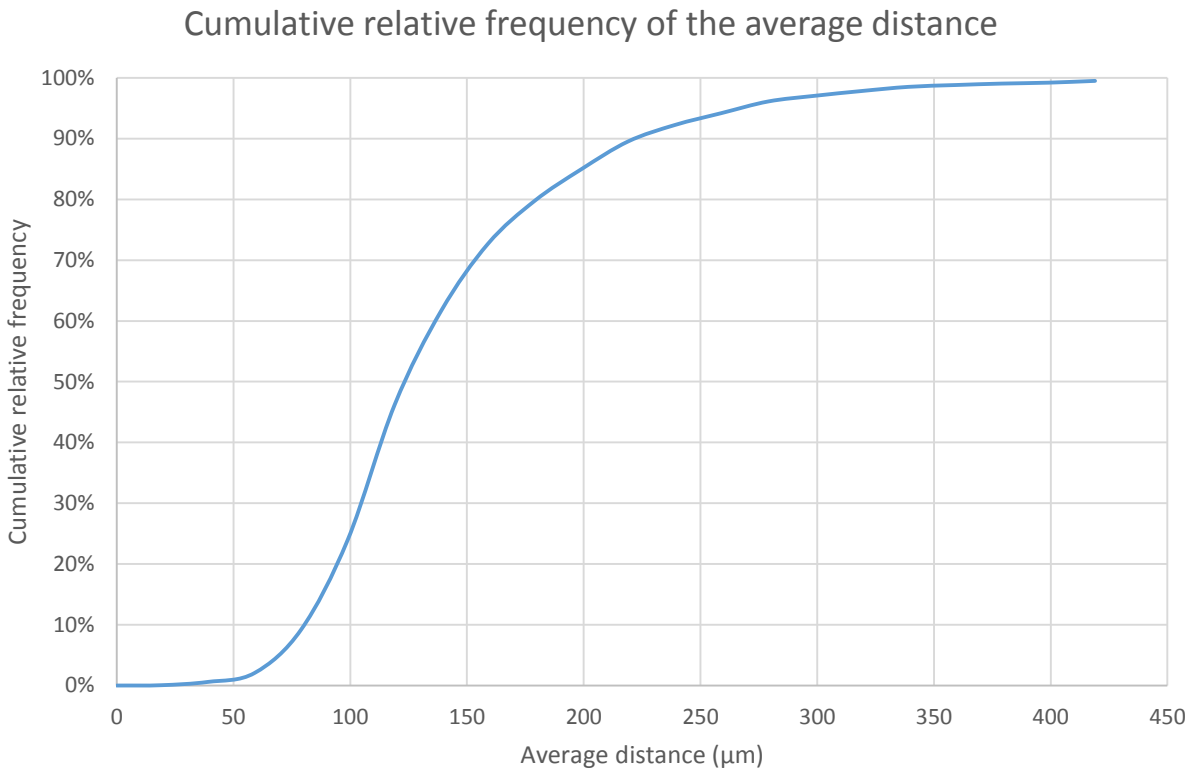

Figure 4.4: Cumulative relative frequency of the average distance of B4.

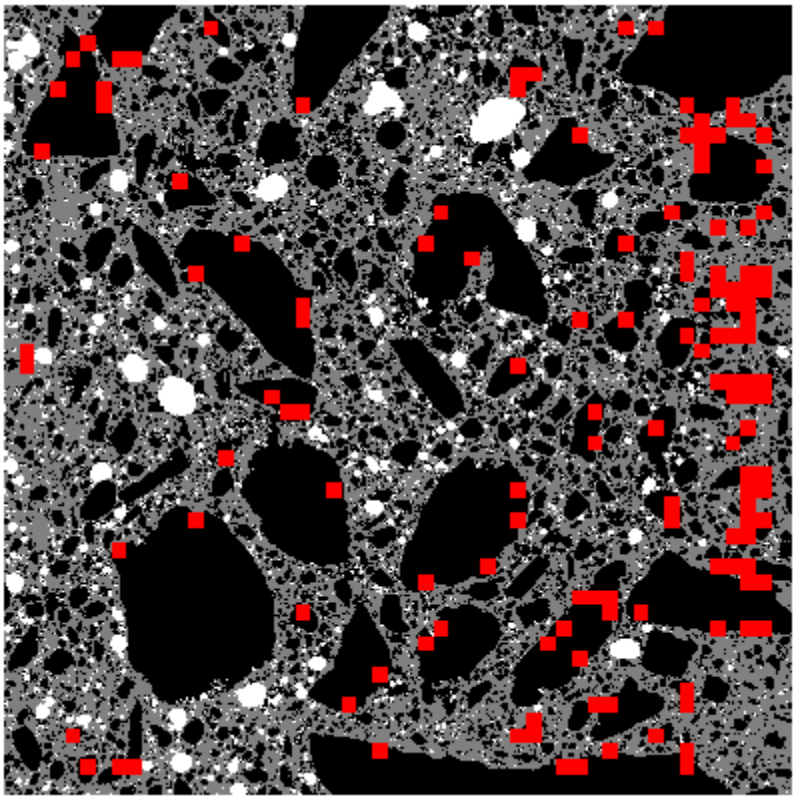

Figure 4.5: Easily damaged areas of B4.

Besides the areas on the edge of some coarse aggregates, the red areas locate where fine aggregates and pastes crowd together without enough entrained air. In Figure 4.6, the magnified areas with the average distance larger than 250 μm are shown.

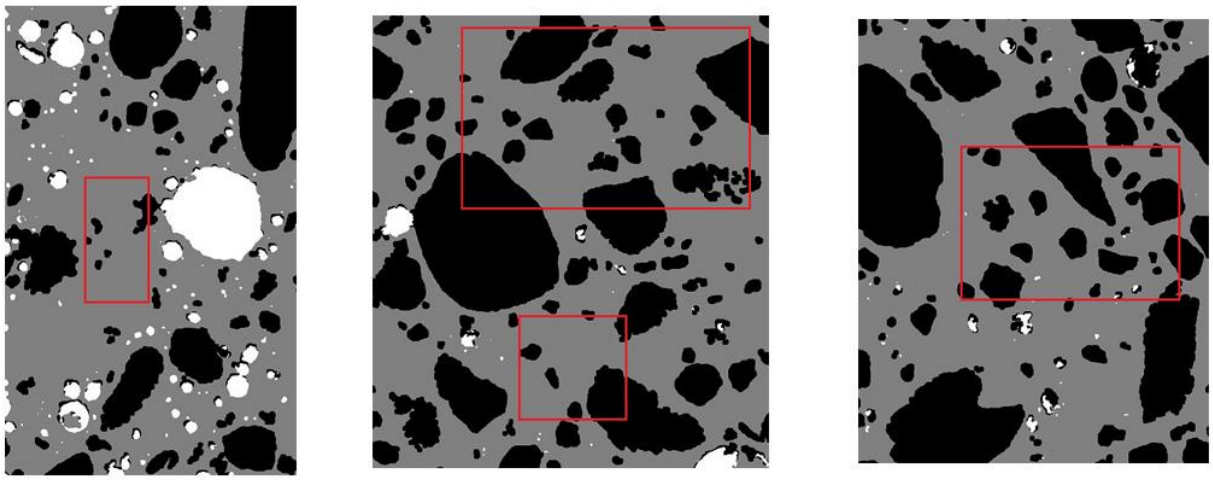

Figure 4.6: Magnified easily damaged areas of B4.

Sample A1 to A4, B1 to B3, E1, E2, E4, and F1 to F4 are all analyzed to obtain the cumulative relative frequency of the average distance and the new spacing factor. The cumulative relative frequency curve will be shown in Appendix C, while the spacing factor will be summarized in Table 4.2. In Table 4.2, the spacing factor according to ASTM C457 will also be shown for comparison. It can be observed in Figure 4.7 that spacing factor in ASTM C457 is always larger than the average distance for a given sample. The method in ASTM C457 to determine the spacing factor is based on one-dimensional chord line calculation so that the air voids that are not traversed are ignored for protection on the cement pastes. Thus, the spacing factor in ASTM C457 is higher and the freezing and thawing resistance for the concrete samples is underestimated.

Table 4.2: Comparison of spacing factor in ASTM C457 and average distance.

Sample	Spacing Factor in ASTM C457 (inch)	Average distance (μm)	(inch)
A1	0.0059	150.53	0.0059
A2	0.0050	118.03	0.0046
A3	0.0058	122.15	0.0048
A4	0.0071	125.26	0.0049
$A_{Average}$	0.0059	128.99	0.0051
B1	0.0064	126.13	0.0050
B2	0.0066	142.14	0.0056
B3	0.0071	112.35	0.0044
B4	0.0075	135.72	0.0053
$B_{Average}$	0.0069	129.08	0.0051
E1	0.0049	95.99	0.0038
E2	0.0059	129.72	0.0051
E3	0.0054	101.38	0.0040
E4	0.0060	111.42	0.0044
$C_{Average}$	0.0055	109.63	0.0043
F1	0.0024	81.72	0.0032
F2	0.0039	71.61	0.0028
F3	0.0050	95.98	0.0038
F4	0.0050	86.68	0.0034
$D_{Average}$	0.0041	84.00	0.0033

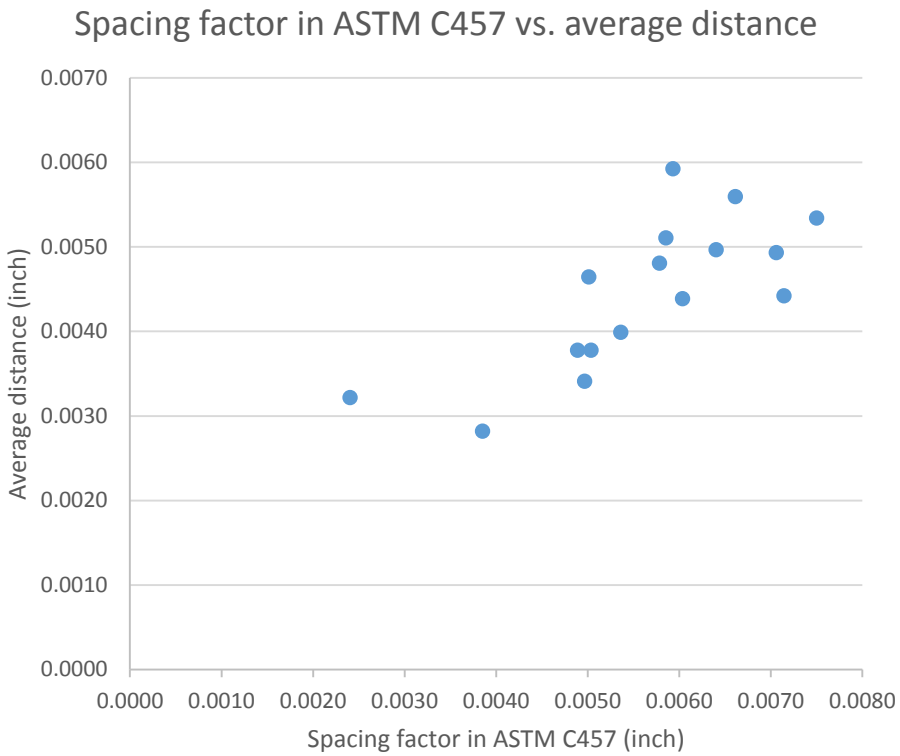

Figure 4.7: Comparison of spacing factor in ASTM C457 and average distance.

The average air content versus the average distance for each sample group is shown in Table 4.3. It can be seen that even though the air content of two samples are similar, the average distance may be different. Moreover, the sample whose air content is lower may also have lower average distance. Therefore, air content alone is insufficient to estimate the freezing and thawing resistance.

Table 4.3: The average air content versus the average distance for each sample group.

Sample	Air content (%)	Average distance (μm)
$A_{Average}$	7.75	128.99
$B_{Average}$	6.96	129.08
$C_{Average}$	5.04	109.63
$D_{Average}$	6.35	84.00

4.3 Protected Paste

Based on stereology relationships, the volume of paste within a distance from air voids in a unit volume can be determined by the average area ratio of paste on the sectional probes. Matlab was used to measure the distance from every paste pixel to the nearest air void. According to ASTM C457, a maximum value of 200 μm for the spacing factor is an appropriate criteria for moderate exposure to freezing and thawing of concrete. Therefore, 200 μm is selected as the distance from the periphery of air voids and the paste within the distance to be assumed to be protected by the air voids. The area fraction of the protected paste can be calculated by the ratio of the number of pastes pixels within the distance to the total number of paste pixels. In Table 4.4, the area fraction of the protected paste is shown for the samples from CTLGroup. The specific surface calculated according to ASTM C457 is also presented in Table 4.4. With larger specific surface of air voids, the fraction of pastes within the selected distance from air voids should increase at the same time. In Figure 4.8, the relationship between the fraction of protected pastes and the specific surface in ASTM C457 is shown for the samples from CTLGroup.

Table 4.4: Area fraction of the paste within 200 μm from air voids.

Sample	Specific Surface in ASTM C457 (1/inch)	Protected paste (%)
A1	749.31	77.88%
A2	663.99	87.10%
A3	732.58	89.92%
A4	664.95	86.78%
$A_{Average}$	702.71	85.42%
B1	691.73	87.12%
B2	651.32	81.07%
B3	692.74	92.28%
B4	698.09	82.80%
$B_{Average}$	683.47	85.82%
E1	879.01	93.81%
E2	1071.51	85.51%
E3	1030.63	94.70%
E4	839.95	91.73%
$C_{Average}$	955.27	91.44%
F1	1462.17	98.03%
F2	858.80	98.88%
F3	1081.77	94.95%
F4	1053.69	96.54%
$D_{Average}$	1114.11	97.10%

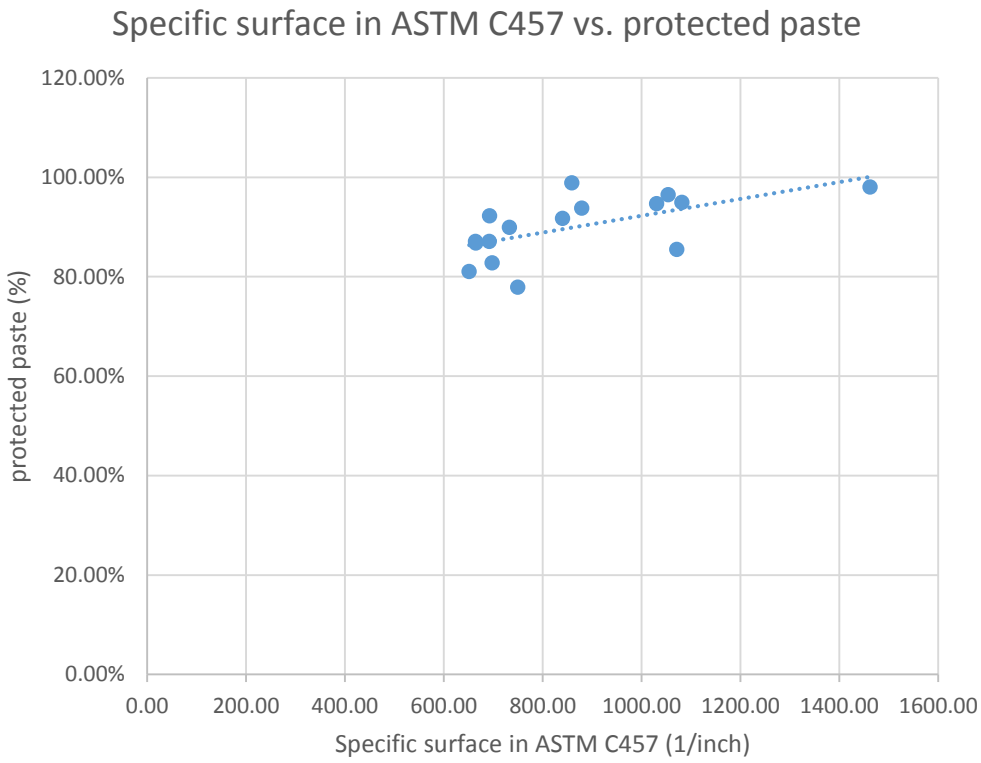

Figure 4.8: Relationship between the specific surface and protected paste.

From Figure 4.8, the correlation is shown between the percentage of protected paste and the conventional specific surface. The points are distributed intensively within the vicinity of the trend line. If the area fractions of protected pastes and the specific surfaces are averaged for Group A, B, E, and F, a good correlation is illustrated in Figure 4.9. Although the area fraction is only a two-dimensional parameter indicating the true three-dimensional property, it loses less information than the one-dimensional parameter like the specific surface since the specific surface is calculated based on average chord length in ASTM C457.

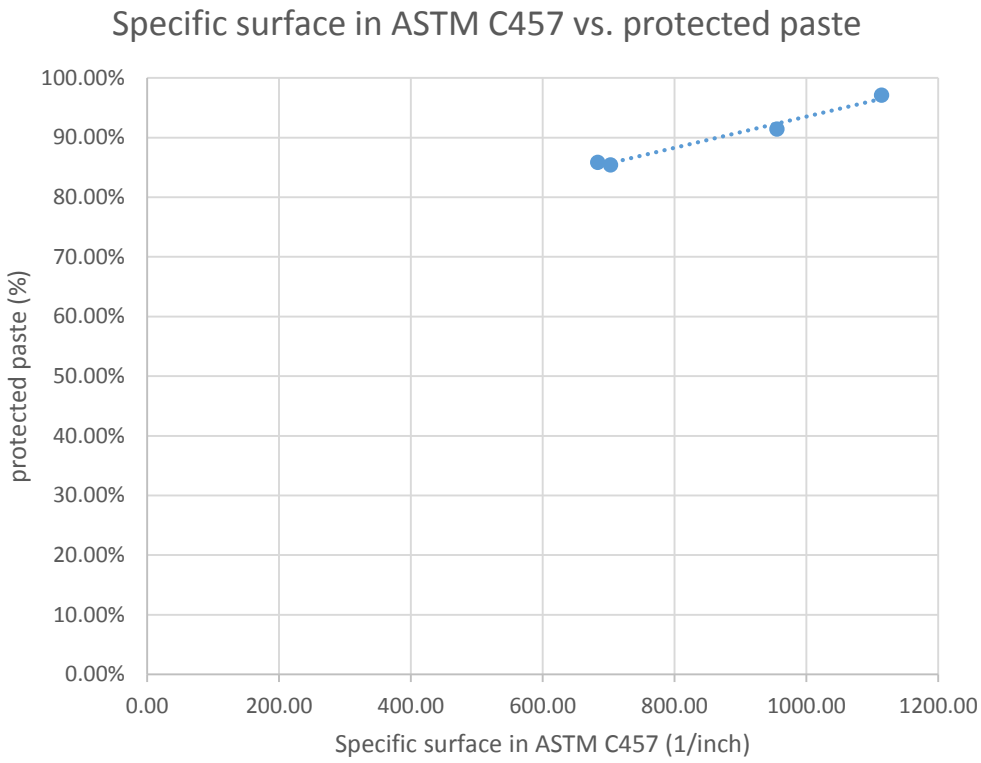

Figure 4.9: Relationship between the average specific surface and average protected paste for Group A, B, E, and F.

4.4 Area Fraction of Air Voids

The air content in volume of hardened concrete is represented by the ratio of the traverse length through air voids to the total length of the linear probes in ASTM C457. If the amount of sampling is large enough or the length of the linear probes is long enough in this case, the margins of error will be controlled properly. Since the area fraction of air voids can be determined easily and conveniently using the scanning image along with its three-phase image, the air content can be represented by the area fraction of air voids on the image. In Table 4.5, the comparison of the air content in ASTM C457 and area fraction of air voids on the scanning image of samples from CTLGroup is shown. It can be seen that the error between the one-

dimensional and two-dimensional parameter is small when the amount of sampling is large enough.

Table 4.5: Comparison of the air content in ASTM C457 and area fraction of air voids.

Case	Air content in ASTM C457 [%]	Area fraction [%]	Error
A1	6.87	6.88	0.18%
A2	8.97	8.89	0.91%
A3	8.19	8.03	1.96%
A4	6.95	6.94	0.10%
B1	6.56	6.58	0.31%
B2	7.97	8.06	1.18%
B3	7.2	7.10	1.42%
B4	6.12	6.05	1.11%
E1	6.57	6.70	1.94%
E2	3.56	3.61	1.40%
E3	4.78	4.85	1.41%
E4	5.26	5.22	0.81%
F1	6.22	6.23	0.23%
F2	8.88	8.73	1.74%
F3	4.3	4.09	5.12%
F4	6.01	6.01	0.02%

4.5 Surface Area of Air Voids

The surface area of air voids is important to achieve a good freezing and thawing performance for concrete no matter according to the Powers' mechanism or the Chatterji mechanism of freezing action. The larger specific surface, the more water in the paste within a distance from air voids can be sucked into the air voids. Besides, the larger specific surface, the more water can freeze on the inner layer of air voids before the unfrozen water is stopped flowing into the air voids. The true surface area of air voids is a three-dimensional property of hardened concrete and the relationship between the specific surface and an estimate with a two-dimensional probe, a

section has to be constructed. According to the results from West [24], the surface area of air voids in a unit volume of hardened concrete can be determined by the ratio of the perimeter of air voids on the section to the total area of the section, which is shown in Equation 31.

$$S_V = \frac{4}{\pi} \times P_A \tag{31}$$

Where S_V is the surface area of air voids in a unit volume of hardened concrete and P_A is the ratio of the perimeter of air voids on the section to the total area of the section.

The results of the perimeter and the resulting surface area of air voids in a unit volume for samples from CTLGroup are shown in Table 4.6. The calculated specific surface in ASTM C457 for these samples is also shown.

Table 4.6: Comparison of specific surface in ASTM C457 and surface area of air voids in a unit volume.

Case	Specific Surface in ASTM C457	Perimeter	Surface area
	1/inch	inch	1/inch
A1	749.3	162.1	53.3
A2	664.0	187.6	61.7
A3	732.6	181.5	59.6
A4	665.0	145.7	47.9
$A_{Average}$	702.7	169.2	55.6
B1	691.7	138.9	45.6
B2	651.3	153.6	50.5
B3	692.7	149.1	49.0
B4	698.1	134.5	44.2
$B_{Average}$	683.5	144.0	47.3
E1	879.0	179.4	59.0
E2	1071.5	115.8	38.1
E3	1030.6	148.4	48.8
E4	839.9	135.6	44.5
$C_{Average}$	955.3	144.8	47.6
F1	1462.2	229.6	75.4
F2	858.8	279.1	91.7
F3	1081.8	138.4	45.5
F4	1053.7	193.8	63.7
$D_{Average}$	1114.1	210.2	69.1

The relationship between specific surface in ASTM C457 and the surface area of air voids in a unit volume of hardened concrete can be illustrated in Figure 4.10. The specific surface in ASTM C457 is defined as “the surface area of the air voids divided by their volume” [2] and it indicates the size of air bubbles. However, the specific surface does not consider the interval between air voids and it is not a parameter associated with the mechanism of freezing. Instead, surface area of air voids in a unit volume of hardened concrete evaluates the amount of water

that can be sucked into air voids along with the amount of pastes that can be protected. Therefore, surface area of air voids in a unit volume can be utilized to represent the freezing and thawing performance of concrete directly.

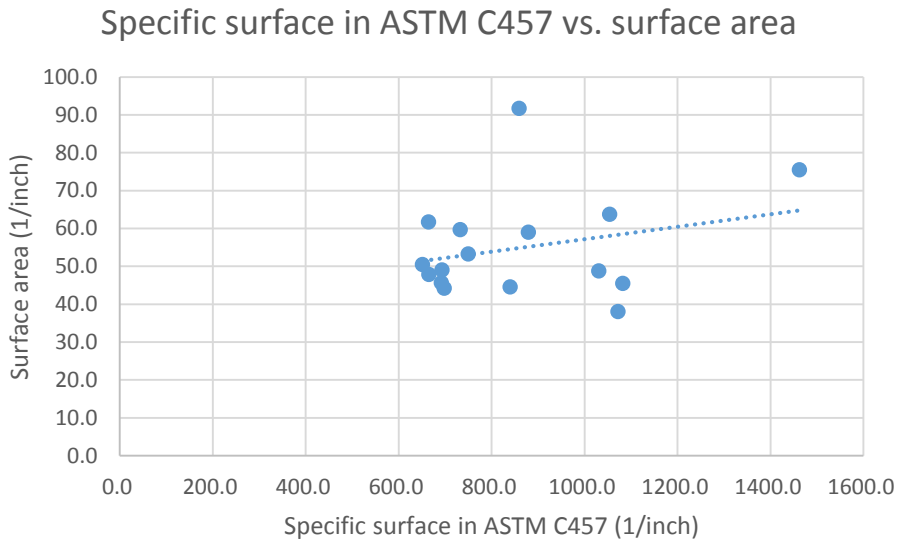

Figure 4.10: Relationship between specific surface in ASTM C457 and surface area of air voids.

In Figure 4.11, the specific surfaces and surface areas of air voids in a unit volume are averaged for Group A, B, E, and F and the discreteness of the points decreases. The specific surface could be expected to increase with the increasing air content and the surface area of air voids in a unit volume also increases with the air content. Then, a correlation between specific surface in ASTM C457 and surface area of air voids in a unit volume should exist as shown in Figure 4.11.

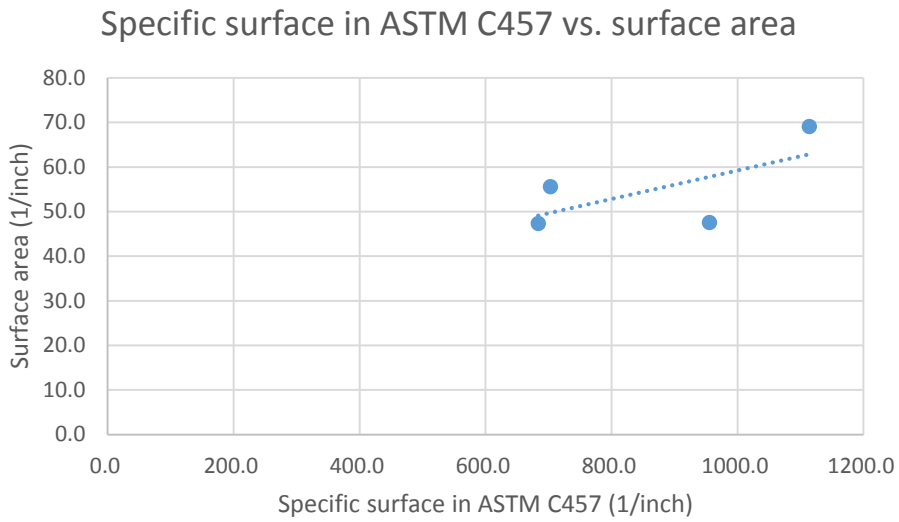

Figure 4.11: Relationship between the average specific surface and average surface area for Group A, B, E, and F.

Chapter 5. Conclusions

This study has developed new techniques and improved existing methods for measuring the parameters of the air-void system. With the ASTM C457 test method serving as a reference, new techniques and automated methods have been developed to acquire and analyze images of polished sections of concrete. Specimen preparation methods were refined, using phenolphthalein to stain the paste and an orange powder to fill air bubbles and provide high brightness and image contrast. A high resolution flatbed scanner was used for image acquisition, and procedures were developed so that a single image could be used for all aspects of analysis. This key advancement makes image acquisition faster and avoids error arising from registration of multiple images. Image processing methods using ImageJ, Photoshop, and Matlab were developed.

The structure of the air-void system in hardened concrete mixed with air-entraining admixtures is critical for the frost resistance of concrete. Mechanisms of freezing and thawing damage have been explained by hydraulic pressure theory, energy of solidification theory, osmotic pressure theory, Litvan's theory, Chatterji's theory, crystallization pressure theory, and cryo-suction theory. Many contradictions between these theories exist, but in many respects, these theories complement each other. Although debate continues regarding Powers hydraulic pressure theory, the spacing factor proposed by Powers is today one of the most widely used parameters to characterize the air-void system, and it has been demonstrated to be successful in practical work. Many spacing factor equations including Powers equation have proposed to characterize the true spacing of the air voids in hardened concrete, and this will be a subject of research for years to come.

A “blind study” was completed to validate the new methods using ASTM C457 results as a reference. The study demonstrated that new automated techniques could provide results comparable to the traditional ASTM C457 test method while opening the door to two-dimensional analysis.

This study proposes new two-dimensional parameters including the average distance of pastes to the nearest air void, the percentage of protected pastes, the area fraction of air voids, and the surface area of air voids. These parameters improve upon simple one-dimensional parameters for addressing models and mechanisms of freezing and thawing performance of concrete. The three-phase image obtained from the automated method makes it possible to determine these parameters by dealing with the polished concrete sections. The relationships between these two-dimensional parameters and the actual freezing and thawing performance should be the subject of research in the future.

The methods in this study have limitations, and thus future work in this area is encouraged. Aggregate porosity – particularly lightweight aggregates – remains a challenge for automated segmentation of phases. Pore spaces such as air bubbles, air voids, and aggregate pores are difficult to differentiate using automated methods. Further software and hardware development may overcome these challenges in the future. Fortunately, these same factors can be shown to have relatively low influence on the measured parameters of the air-void system, and the averaged test results may not be greatly affected.

References

[1] Mindess, S, Young, J.F. and Darwin D., (2003) *Concrete*, 2nd ed., Prentice Hall, Upper Saddle River, NJ.

[2] ASTM Standard C457, 2012, "Standard Test Method for Microscopical Determination of Parameters of the Air-Void System in Hardened Concrete," ASTM International, West Conshohocken, PA.

[3] Chatterji, S., and Gudmundsson, H., (1977) "Characterization of Entrained Air Bubble System in Concrete by Means of an Image Analysis Microscope," *Cement and Concrete Research*, Vol. 7, No. 4, pp. 423-428.

[4] Pleau, R., Pigeon, M., Laurencot, J. L., (2001) "Some Findings on the Usefulness of Image Analysis for Determining the Characteristics of the Air-void System on Hardened Concrete," *Cement and Concrete Composites*, Vol.23, pp. 237-246.

[5] Zhang, Z., Ansari, F. and Vitillo, N., (2005) "Automated Determination of Entrained Air Void Parameters in Hardened Concrete," *ACI Materials Journal*, Vol. 102, No. 1, Jan.-Feb.

[6] Schlorholtz, S., (1998) *Image Analysis for Evaluating Air Void Parameters of Concrete*, Project HR-396, Final Report. Iowa Department of Transportation, Ames.

[7] Peterson, K. R., Swartz, R. A., Sutter, L. L., and Van Dam, T. L., (2002) "Hardened Concrete Air Void Analysis with a Flatbed Scanner," *Journal of Transportation Research Board*, No. 1775, Transportation Research Board, National Research Council, Washington, D.C., pp. 36-43.

[8] Zalocha, D., Kasperkiewicz, J., (2005) "Estimation of the structure of air entrained concrete using a flatbed scanner," *Cement and Concrete Research*, 35 (10), pp. 2041-2046.

[9] Peterson, K., L. Sutter, and Radlinski, M., (2009) "The Practical of Application a Flatbed Scanner for Air-Void Characterization of Hardened Concrete," *Journal of ASTM International*, Vol. 6.

[10] Peterson, K., J. Carlson, L. Sutter, and Van Dam, T., (2009) "Methods for Threshold Optimization for Images Collected from Contrast Enhanced Concrete Surfaces for Air-Void System Characterization," *Materials Characterization*, Vol. 60, pp. 710-715.

[11] Radlinski, M., Olek, J., Zhang, Q.and Peterson, K., (2010) "Evaluation of the Critical Air-Void System Parameters for Freeze-Thaw Resistant Ternary Concrete using the Manual Point-Count and the Flatbed Scanner Methods," *Journal of ASTM International*, Vol. 7.

[12] Zalocha, D., and Kasperkiewicz, J., "Estimation of the Structure of Air Entrained Concrete Using a Flatbed Scanner," *Cement and Concrete Research*, Vol. 35, 2005, pp. 2041-2046.

[13] Jakobsen, U. H., Pade, C., Thaulow, N., Brown, D., Sahu, S., Magnusson, O., De Buck, S., and De Schutter, G., (2006) "Automated Air Void Analysis of Hardened Concrete - a Round Robin Study," *Cement and Concrete Research*, Vol. 36, pp. 1444-1452.

[14] Ramezanianpour, A. M. and Hooton, R. D., (2010) "Evaluation of Two Automated Methods for Air-Void Analysis of Hardened Concrete," *ASTM Special Technical Publication* Vol. 1511, pp. 27-40.

[15] Ramezanianpour, A. A., Nadooshan, M. J., and Peydayesh, M., (2013) "Effect of New Composite Cement Containing Volcanic Ash and Limestone on Mechanical Properties and Salt Scaling Resistance of Concrete," *Journal of Materials in Civil Engineering*, Vol.25, pp. 1587-1593.

[16] Powers, T.C., (1949) "The air requirement of frost-resistant concrete," *Proceedings of the Highway Research Board*, 29, 184-211.

[17] Powers, T.C. and Helmuth, R.A., (1953) "Theory of volume changes in hardened Portland cement pasts during freezing," *Proceedings of the Highway Research Board*, 32, 285-297.

[18] Powers, T.C., (1975) "Freezing effects in Concrete," *ACI Special Publication* SP-47, American Concrete Institute, Detroit, MI, pp. 1-11.

[19] Litvan, G.G., (1972) "Phase transitions of adsorbates IV — Mechanism of frost action in hardened cement paste," *Journal of the American Ceramic Society*, 55(1), 38-42.

[20] Chatterji, S., (2003) "Freezing of air-entrained cement-based materials and specific actions of air-entraining agents," *Cement Concrete Composite*, 25 (7) pp. 759–765.

[21] Scherer, G.W. and Valenza II, J.J., "Mechanisms of Frost Damage," *Materials Science of Concrete*, Vol. VII, pp. 209-246.

[22] Coussy, Olivier, Monteiro, Paulo, (2008) "Poroelastic model for concrete exposed to freezing temperatures," *Cement and Concrete Research*, Volume 38, Issue 1, Pages 40-48.

[23] West, Mark J., (2012) *Basic Stereology for Biologists and Neuroscientists*, CSHL Press, Cold Spring Harbor, NY, USA.

[24] West, MJ., (1993) "New stereological methods for counting neurons," *Neurobiol Aging*, 14, 275–285.

[25] Defay, R. and Prigogine, I., (1966) *Surface Tension and Adsorption*, Wiley, New York.

[26] Brun, M., Lallemand, A., Quinson, J.F., Eyraud, C., (1977) "A new method for the simultaneous determination of the size and the shape of pores: the thermoporometry", *Thermochimica Acta*, 21, 59-88.

[27] Everett, D.H. and Haynes, J.M., (1965) "Capillary properties of some model system with special reference to frost damage," *RILEM. Bull*., 168, 65-73.

[28] Pigeon, M. and Pleau, R., (1994) *Durability of Concrete in Cold Climates*, Chapman and Hall, London.

[29] Chatterji, S., (1999) "Aspects of freezing process in porous material–water system. Part 2. Freezing and properties of frozen porous materials," *Cement and Concrete Research*, 29,781–4.

[30] Helmuth, RA., (1961) "Dimensional changes of hardened Portland cement pastes caused by temperature changes," *Proceedings of Highway Research Board*, 40, 315–36.

[31] Helmuth, RA., (1960) "Capillary size restriction on ice formation in hardened Portland cement pastes," *Proceedings of the IV International Symposium on Chemistry of Cement*, Washington DC, vol. II., p. 855–69.

[32] Helmuth, RA., (1960) "Discussion of the paper 'Frost action in concrete.' by P. Nerenst," *Proceedings of the IV International Symposium on Chemistry of Cement*, Washington DC, vol. II., p. 829–33.

[33] Mielenz, RC., (1968) "Use of surface-active agents in concrete," *Proceedings of the V International Symposium on Chemistry of Cement*, Tokyo, Part IV. p. 1–102.

[34] Chatterji, S., (1984) "The spacing factor in entrained air-bubbles. Has it any significance?" *Cement and Concrete Research*, 14,757–8.

[35] ASTM C233, 2011, "Air-entraining admixtures for concrete. American Society for Testing Materials," ASTM International, West Conshohocken, PA.

[36] ASTM C260, 2010a, "Standard specification for air-entraining admixtures for concrete," American Society for Testing Materials, ASTM International, West Conshohocken, PA.

[37] Monteiro, P.J.M., Coussy, O., Silva, D. A., (2006) "Effect of cryo-suction and air void transition layer on hydraulic pressure of freezing concrete," *Materials Journal, ACI*, 103 (2) 136–140.

[38] Weibel, ER., (1979) *Stereological methods Vol 1: Practical methods for biological morphometry,* Academic Press, London.

[39] Delesse, MA., (1847) "Procédé mécanique pour déterminer la composition des roches," *Comptes Rendus de l'Académie des Sciences*, 25, 544–545.

[40] Rosiwal, A., (1898) "Über geometrische Gesteinsanalysen," *Verhandl der KK Geol*.

[41] Thomson, E., (1930) "Quantitative microscopic analysis," *The Journal of Geology*, 38, 193–222.

[42] Philleo, R.E., (1983) "A method for analyzing void distribution in air-entrained concrete," *Cement and Concrete Aggregates*, 5, 128-130.

[43] Attiogbe, E.K., (1993) "Mean spacing of air voids in hardened concrete," *ACI Materials Journal*, 90, 174-181.

[44] Underwood, E.E., (1970) *Quantitative Stereology*, Addison-Wesley, Reading.

[45] Pleau, R. and Pigeon, M., (1996) “The use of the flow length concept to assess the efficiency of air entrainment with regards to frost durability: Part - Description of the test method,” *Cement and Concrete Aggregates*, 18, 19-29.

Appendix A. Experimental Procedure of the Automated Measurement of the Parameters of Air-void System

Sample Preparation

The procedures to prepare samples for scanning reflect guidance and recommendations from other researchers, including Kyle Riding (KSU), Karl Peterson (Toronto), and Kim Kurtis (Gatech).

Sectioning:

Cut a sample that is of uniform thickness (about 2 inches) using a concrete saw. It is important for the subsequent polishing process to cut a sample of uniform thickness since fewer and shallow scratches from the saw cut lead to less effort in the first polishing step. During the cut, water is used to move the dirt from the sample.

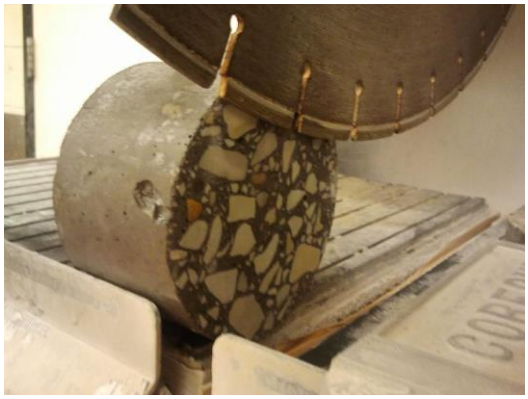

Figure A.1: (Left) Concrete saw; (Right) Cut a sample with uniform thickness.

Air Void Protection:

After washing the sample from sectioning with water, apply lacquer to the surface and let dry to protect the air voids on the surface. In order to check if the sample is polished uniformly, draw circles on the sample using a construction crayon before polishing.

Figure A.2: Air void protection.

Sample Holder Frame:

A wooden frame is made to hold samples and the holes in the frame are slightly larger than 4-inch diameter cylinders. Bearings and rollers are fixed underneath the frame to help samples in rotating during polishing so that a smooth and uniform polishing surface is obtained. Samples are required to rest higher than the level of the rollers in order to ensure contact between the samples and rollers. The positions of the rollers need to be determined by iterative trial to ensure that there is enough room for samples to rotate.

Figure A.3: Sample holder frame.

Polishing:

An 18 inch lapping wheel is used to polish samples; in this case a model ASW-1800 manufactured by ASW Diamond. A sequence of lapping disks are attached on the ground steel plate and the polishing protocol is shown below:

60 grit disk (10 minutes)

260 grit disk (10 minutes)

800 grit disk (15-20 minutes)

Wash the samples between polishing steps.

Figure A.4: Polishing.

Cleaning and Checking Flatness:

After all polishing steps, the sample needs to be washed and dried using fan for 20 minutes. Then, soak samples in pure lacquer thinner to remove the lacquer applied before polishing from the air voids. After drying the samples, check the flatness of the surface with a machinist rule. If no light can transmit through the contact surface, the flatness is satisfactory.

Figure A.5: Cleaning and checking flatness.

Staining:

1% solid phenolphthalein is dissolved in a 1:1 solution of methanol and water. Next, the polished surface is stained with phenolphthalein solution using a sprayer. Allow the solution to sit for about 1 min and dry the samples using a fan for 20 min.

Figure A.6: Staining.

Orange-Powder Treatment:

After staining, press orange marking chalk powder gently into the voids using a rubber stopper. Next, scrape away most of the excess powder with a razor blade and wipe away the remaining powder.

Figure A.7: Orange-powder treatment.

Scanning and Registration:

A Canon CanoScan 9000F scanner is used set at the highest resolution 4800 x 4800 dpi (or 5.3 microns per pixel). The sample is placed at the corner of the glass bed, about 1 inch from the two edges. Scan only once and a tiff type image can be obtained. The area is 50×50 mm and image size is about 255 MB. Scanning time is about 2 min.

Figure A.8: Scanning and registration.

Image Processing

For image processing, Photoshop is employed to create an 8-bit image with three phases including air voids in white, aggregate in black, and paste in 50% grey. ImageJ is also used to fill up all the holes in the aggregates within the creation of the 8-bit image. Subsequently, the three-phase image is analyzed and the resulting parameters of air-void system according to the ASTM C457 are written into an Excel spreadsheet. The detailed procedures are shown below.

In the histogram of the original scanning image, narrow the selection to the peak near "255". Then, all the air voids will stand out from the background.

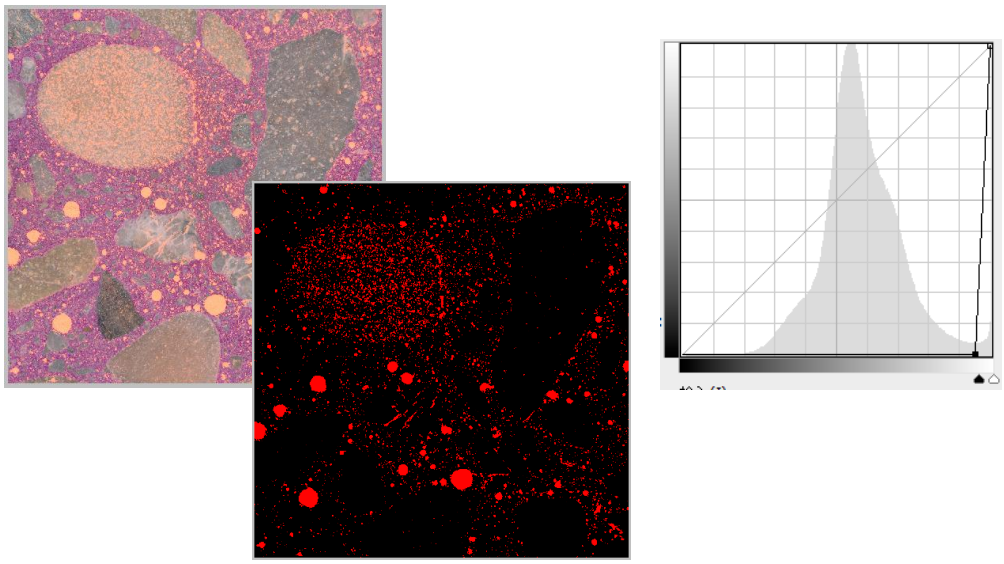

Figure A.9: Histogram of the original scanning image.

Identify the color range of the air void, select and save the area of the air void as a new channel in Photoshop.

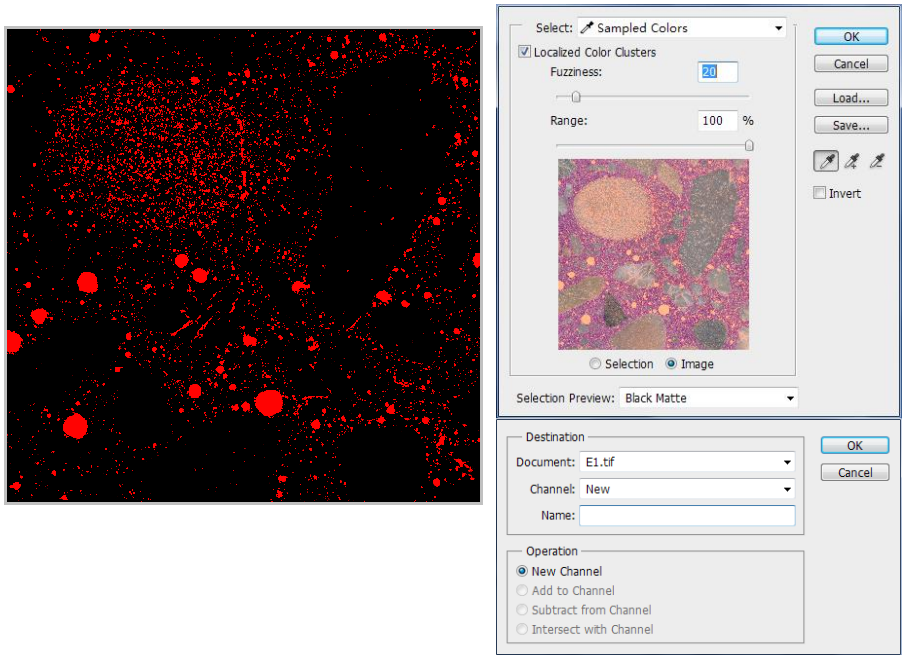

Figure A.10: Identification of the color range of the air void.

Use the channel mixer function to highlight all the air voids and aggregates and under this adjustment, the paste is shown in black. Then, assign a new channel for the selected air voids and aggregates.

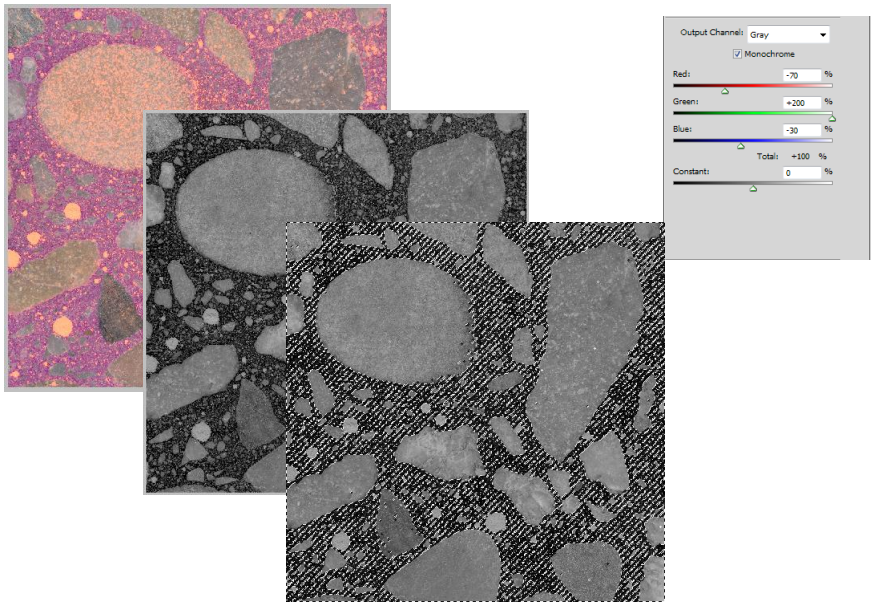

Figure A.11: Highlight of the air voids and aggregates.

Create an 8-bit image and in this image, the selected air voids and aggregates are shown in black. Then, subtract the air voids obtained in previous step from the 8-bit image so as to get a new image only presenting the aggregates.

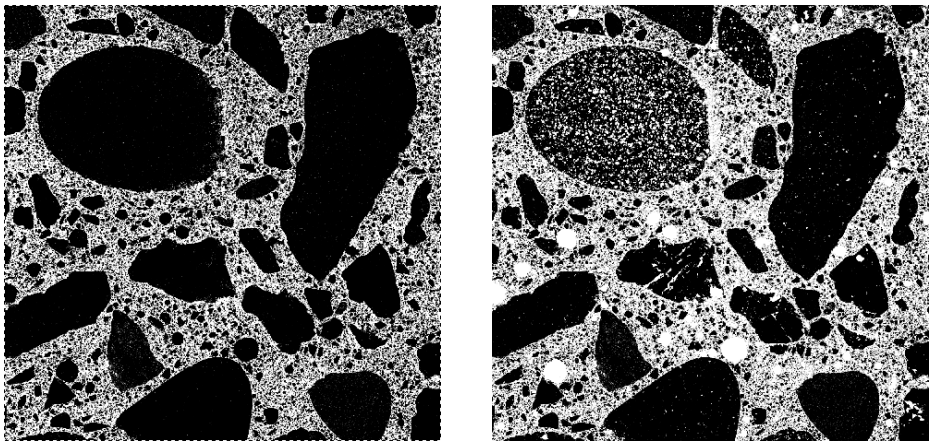

Figure A.12: 8-bit image presenting the aggregates.

Import the new 8-bit image into ImageJ and fill up all the holes in the aggregates. In the filling, set the scale according to the sample conditions and filter out the aggregates less than 10 microns in diameter. Select “Masks” in the dropdown list of “Show” and a new image of aggregates is obtained.

Next, a three-phase image can be created with “air-voids” in white (255), “aggregates” in black (0), and “paste” in 50% grey (128).

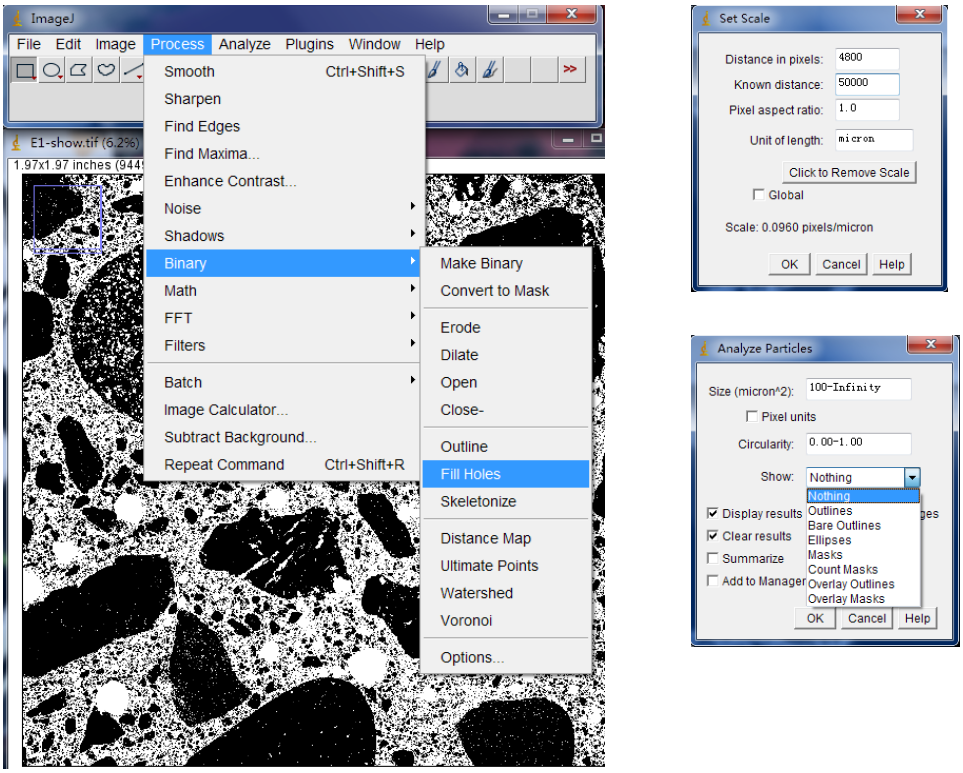

Figure A.13: Creation of a three-phase image.

The three-phase image is imported into Matlab and the resulting parameters of air-void system in the sample according to ASTM C457 are written into an Excel spreadsheet.

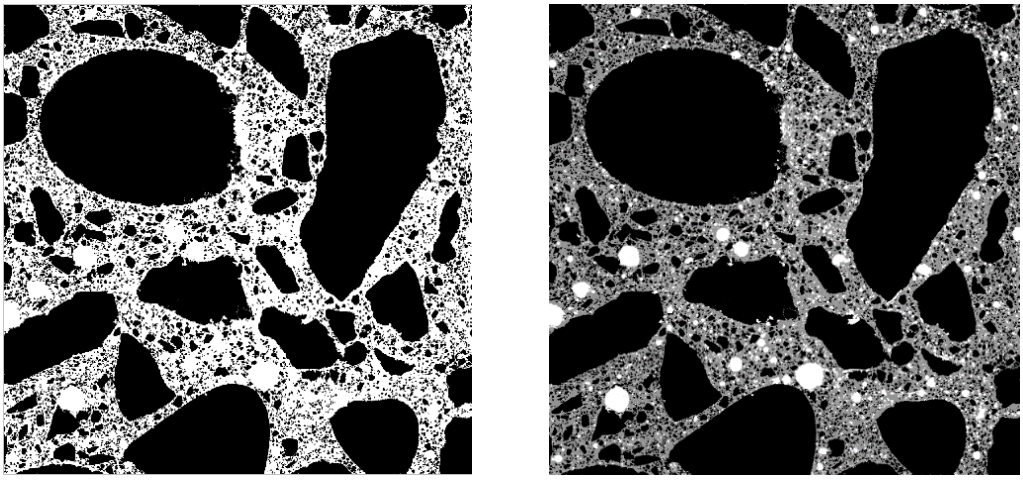

Figure A.14: Calculation of the parameters in ASTM C457 using Matlab.

Appendix B. Original Scanning Images and Three-phase Images

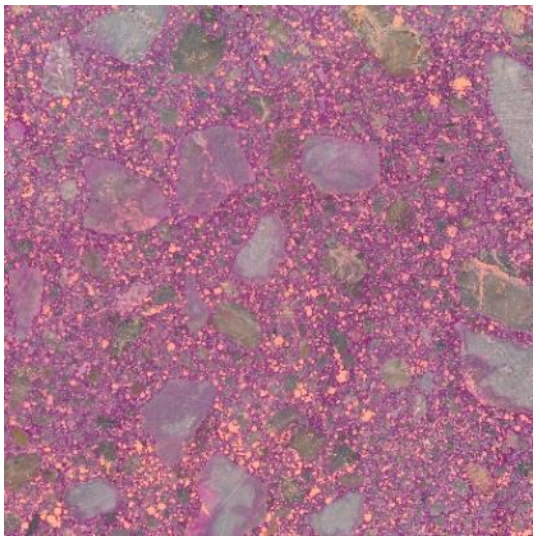

Figure B.1: Scanned photo, A1.

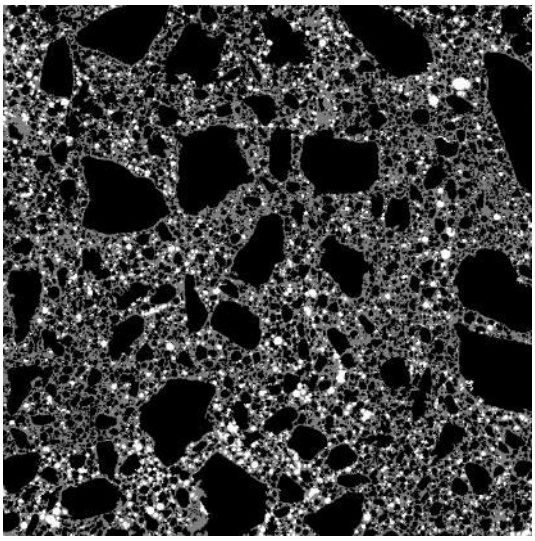

Figure B.2: Three-phase image, A1.

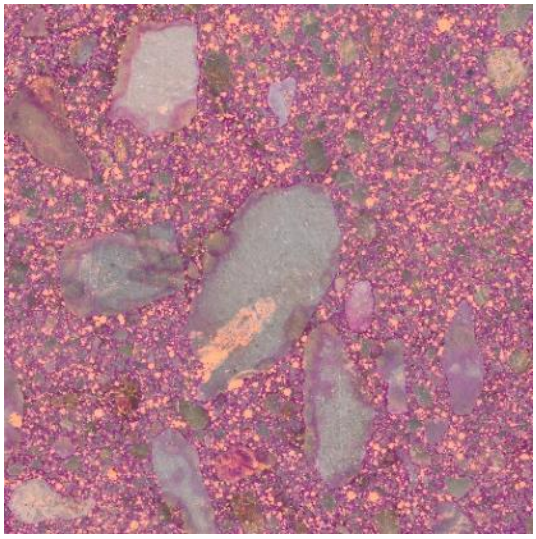

Figure B.3: Scanned photo, A2.

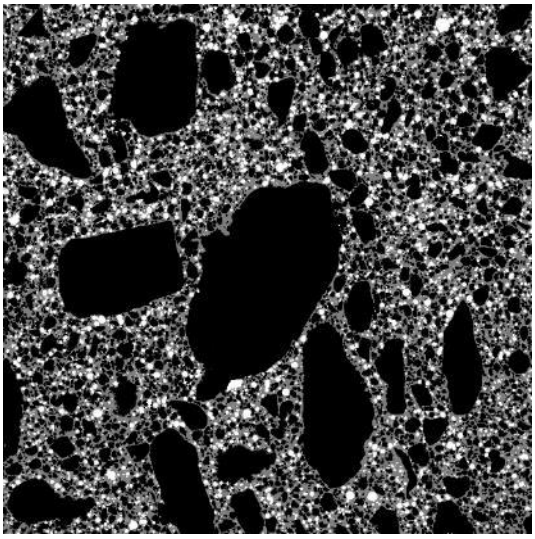

Figure B.4: Three-phase image, A2.

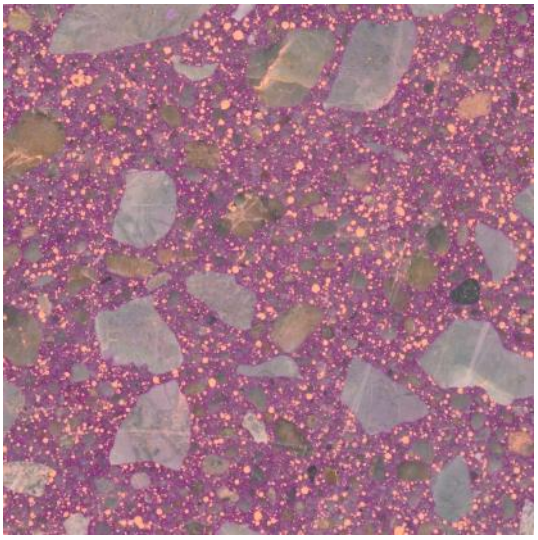

Figure B.5: Scanned photo, A3.

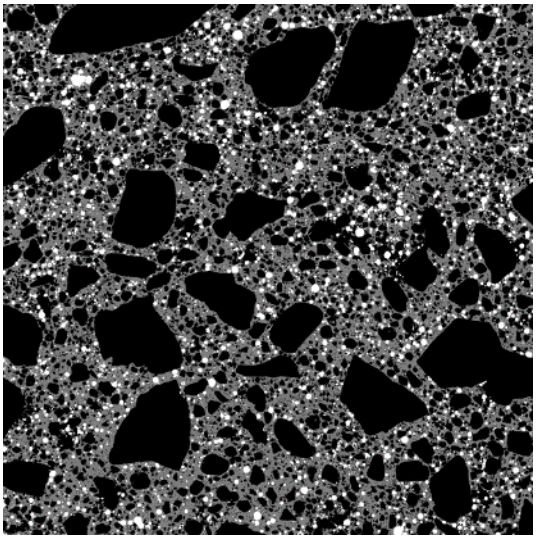

Figure B.6: Three-phase image, A3.

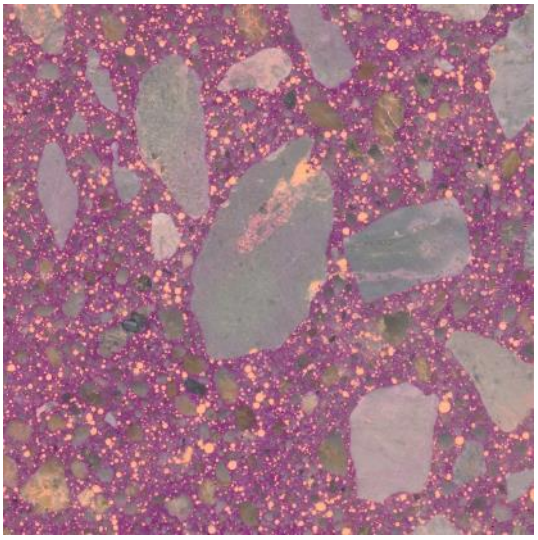

Figure B.7: Scanned photo, A4.

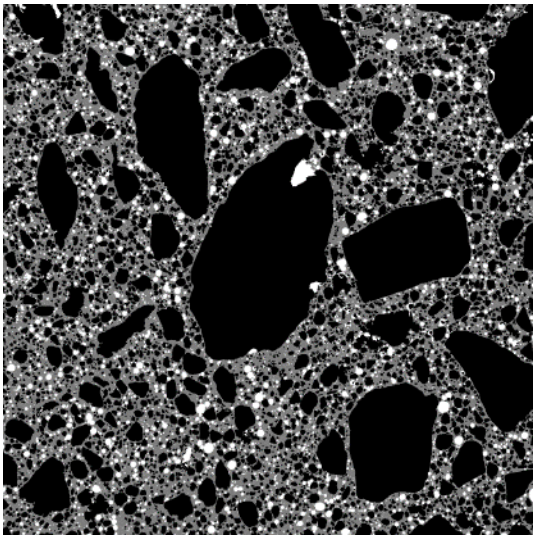

Figure B.8: Three-phase image, A4.

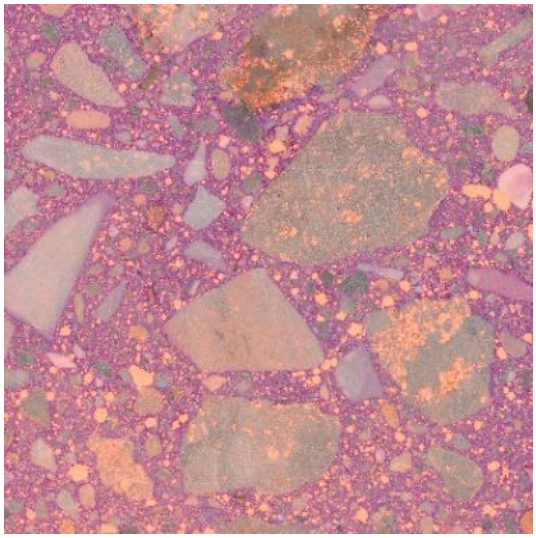

Figure B.9: Scanned photo, B1.

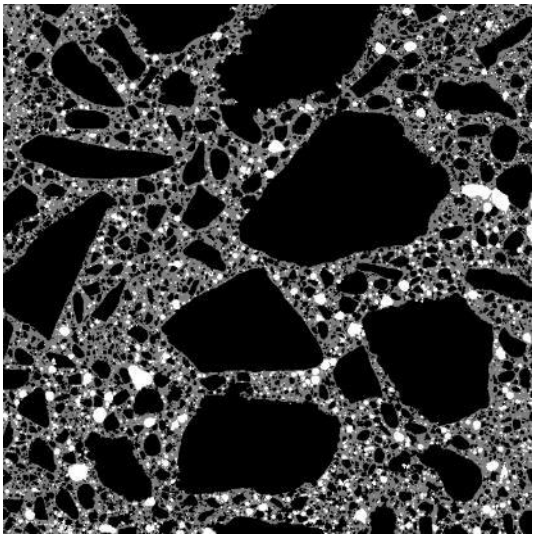

Figure B.10: Three-phase image, B1.

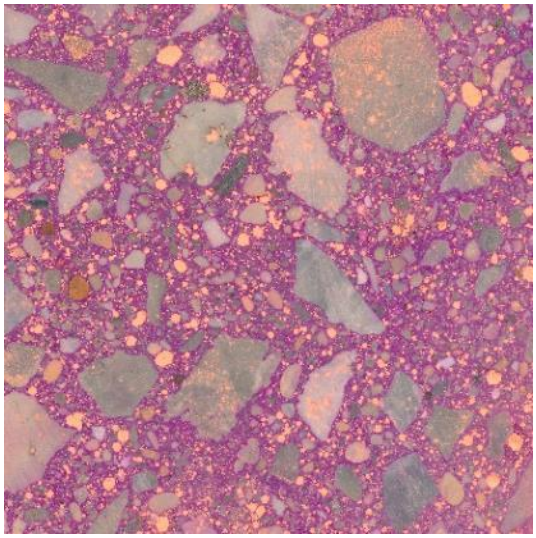

Figure B.11: Scanned photo, B2.

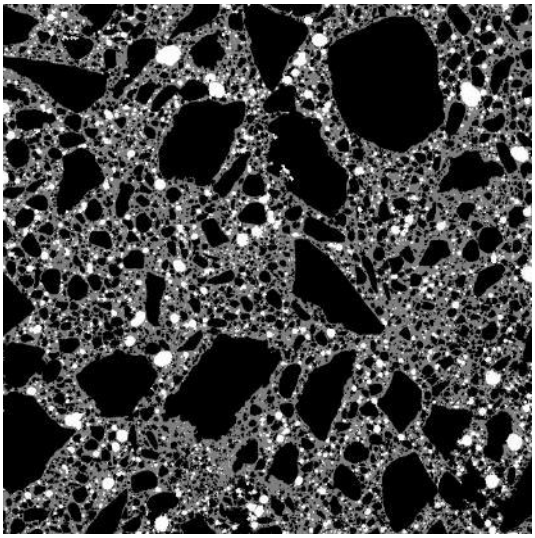

Figure B.12: Three-phase image, B2.

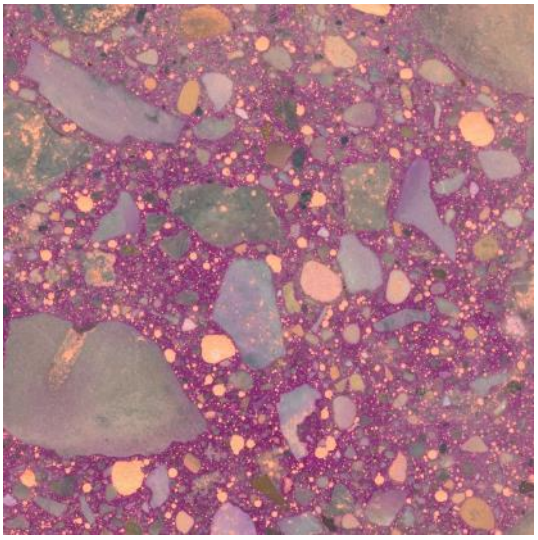

Figure B.13: Scanned photo, B3.

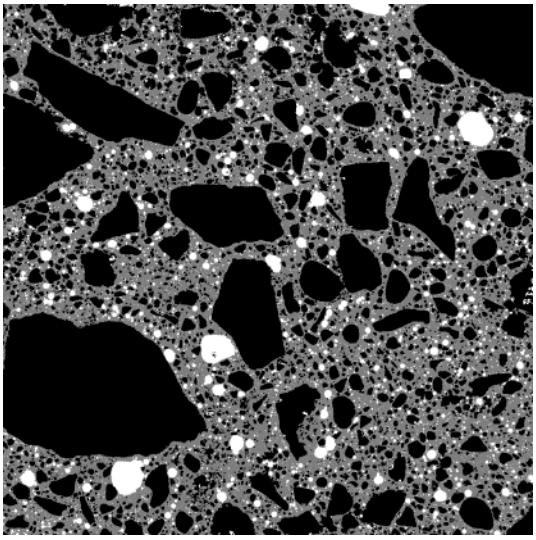

Figure B.14: Three-phase image, B3.

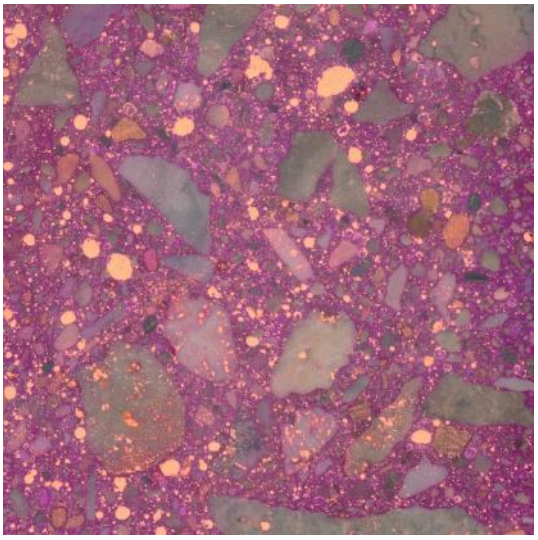

Figure B.15: Scanned photo, B4.

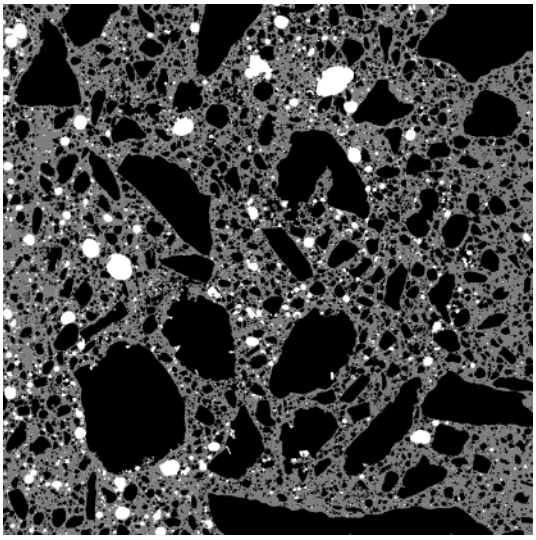

Figure B.16: Three-phase image, B4.

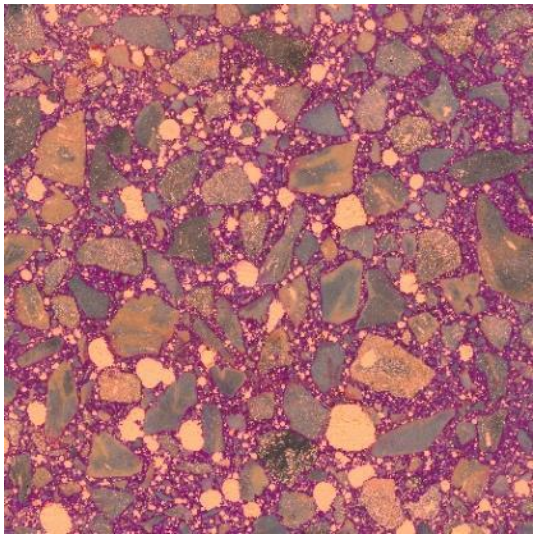

Figure B.17: Scanned photo, C1.

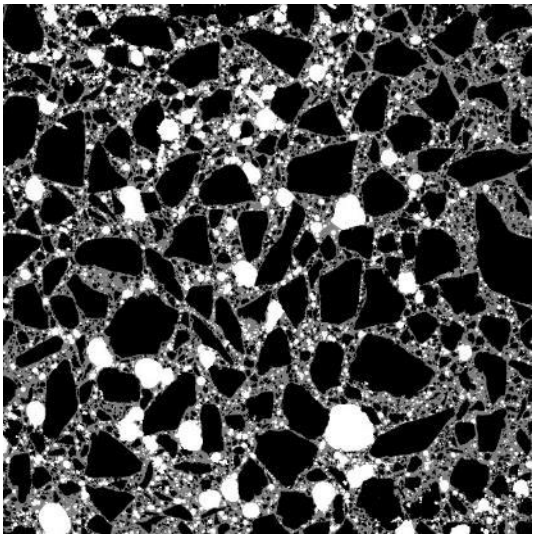

Figure B.18: Three-phase image, C1.

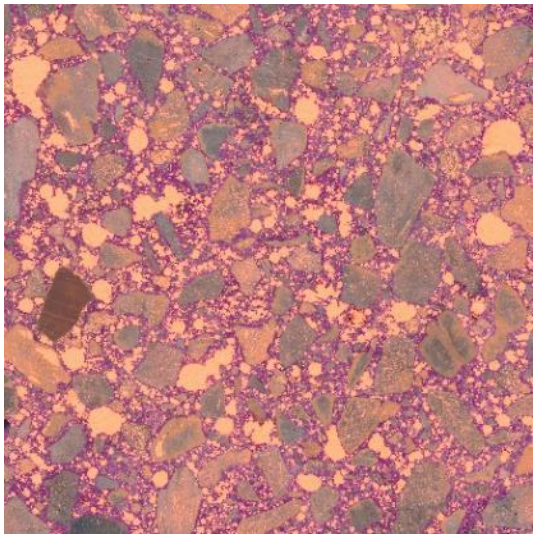

Figure B.19: Scanned photo, C2.

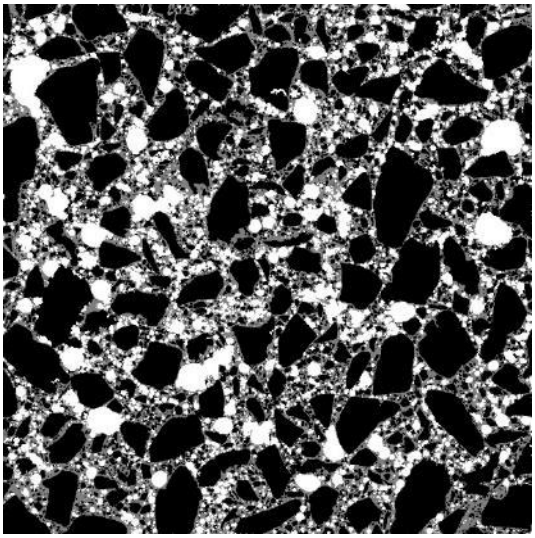

Figure B.20: Three-phase image, C2.

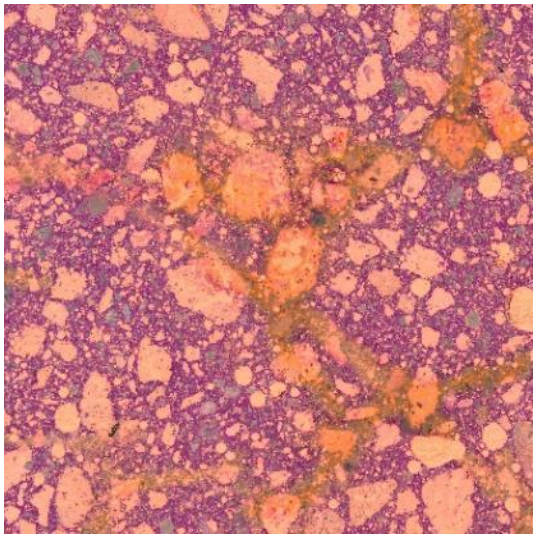

Figure B.21: Scanned photo, D1.

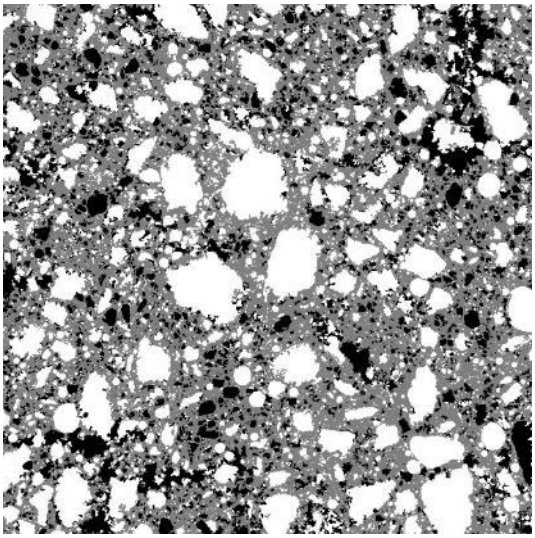

Figure B.22: Three-phase image, D1.

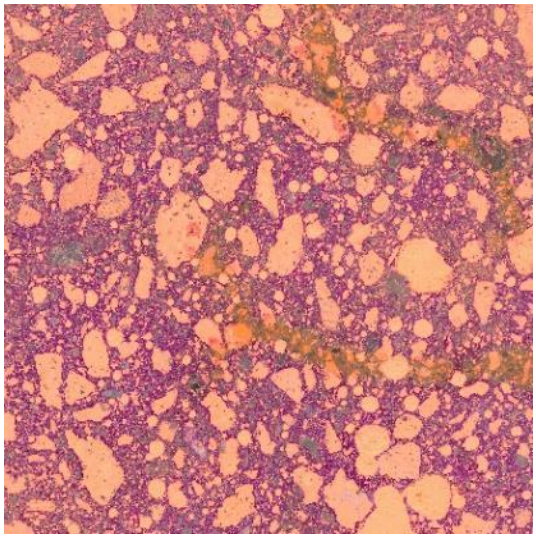

Figure B.23: Scanned photo, D2.

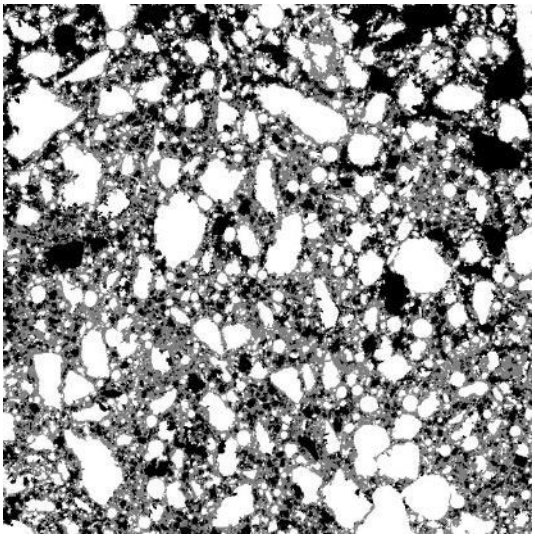

Figure B.24: Three-phase image, D2.

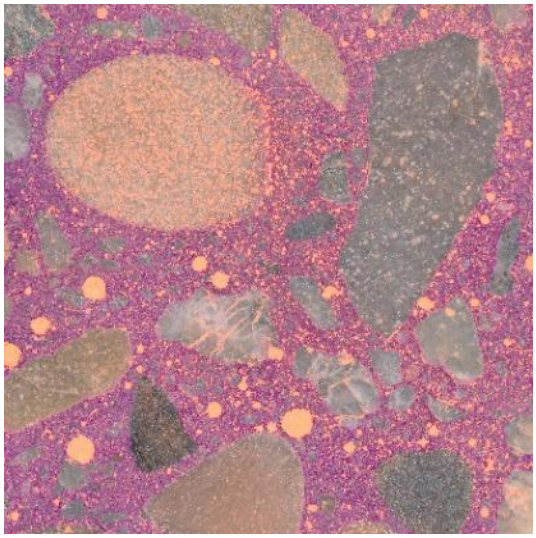

Figure B.25: Scanned photo, E1.

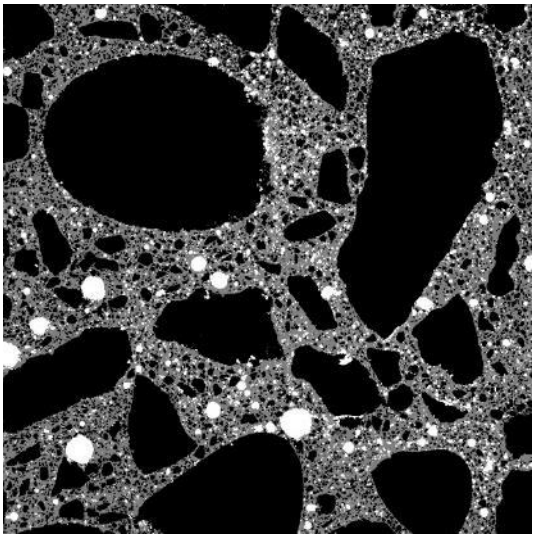

Figure B.26: Three-phase image, E1.

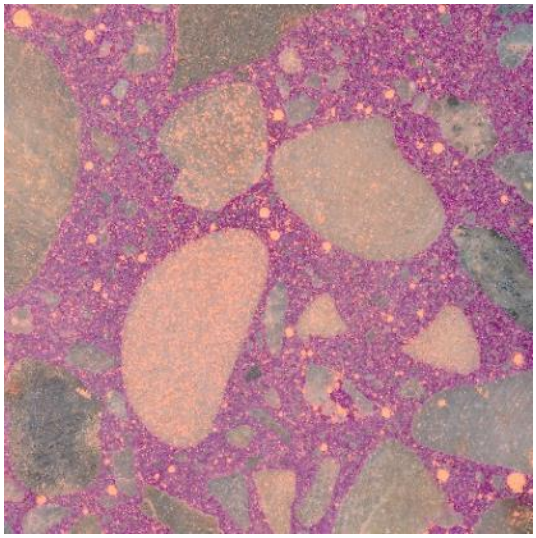

Figure B.27: Scanned photo, E2.

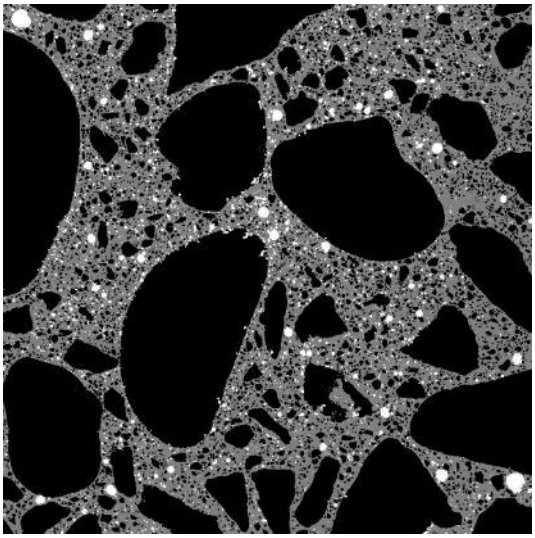

Figure B.28: Three-phase image, E2.

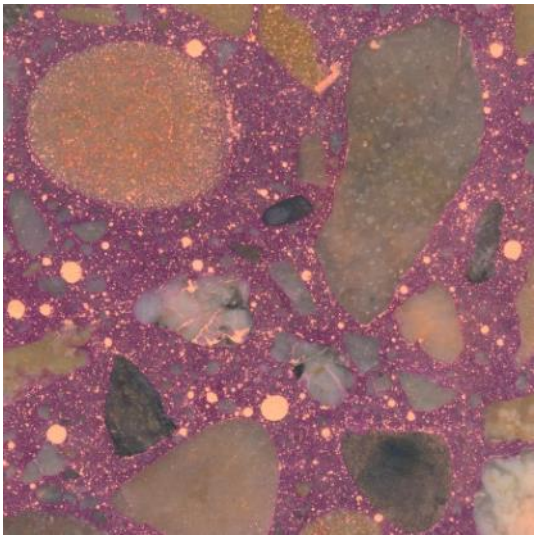

Figure B.29: Scanned photo, E3.

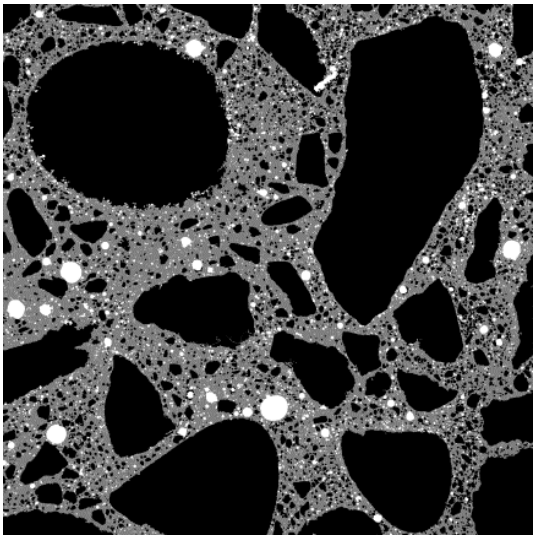

Figure B.30: Three-phase image, E3.

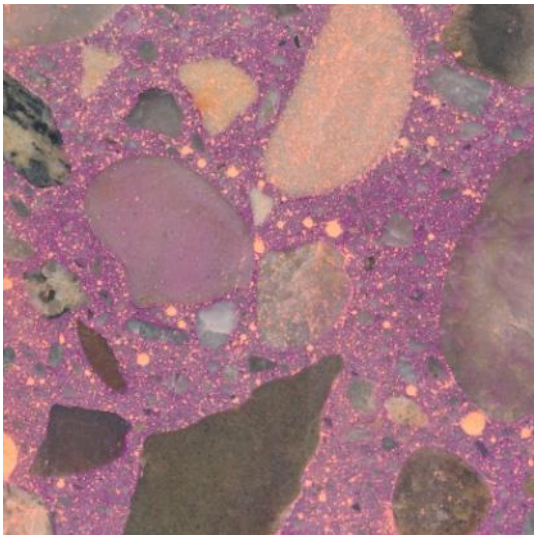

Figure B.31: Scanned photo, E4.

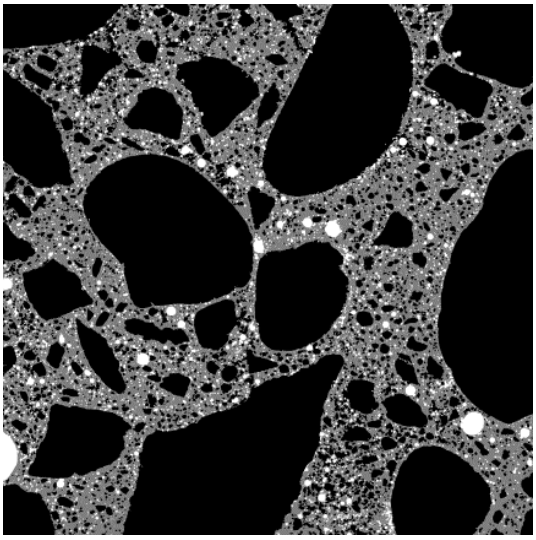

Figure B.32: Three-phase image, E4.

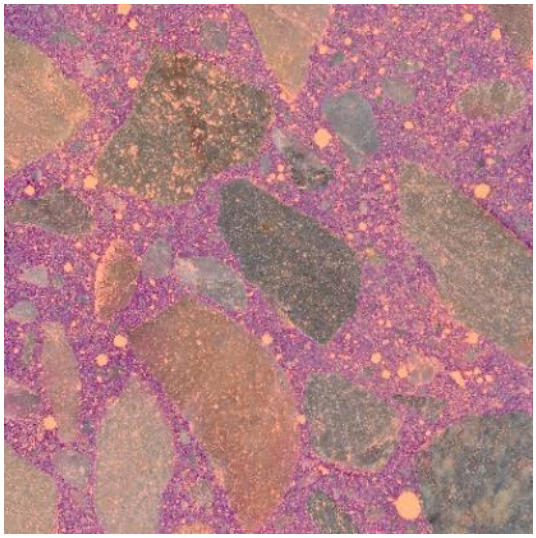

Figure B.33: Scanned photo, F1.

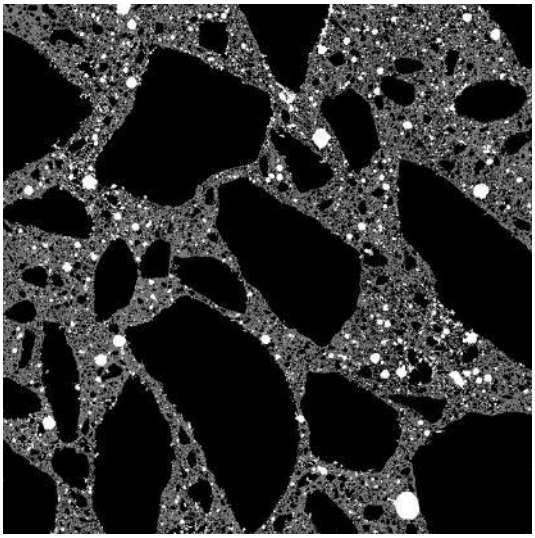

Figure B.34: Three-phase image, F1.

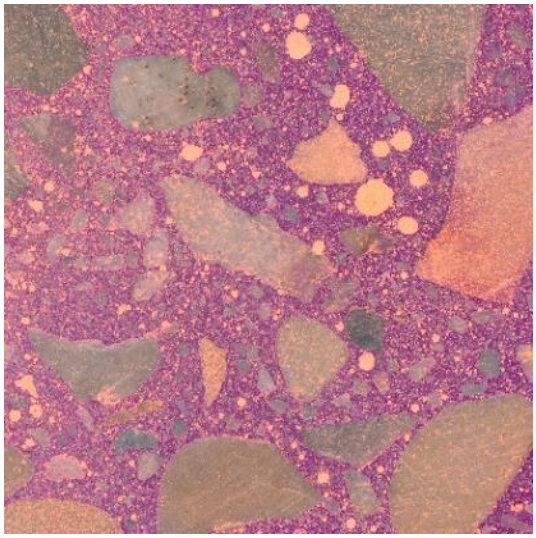

Figure B.35: Scanned photo, F2.

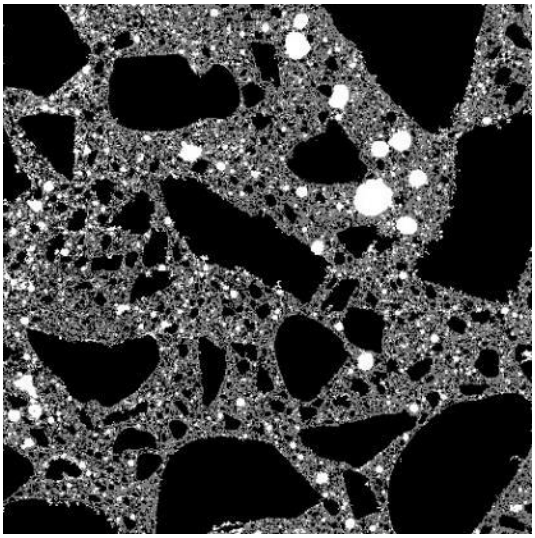

Figure B.36: Three-phase image, F2.

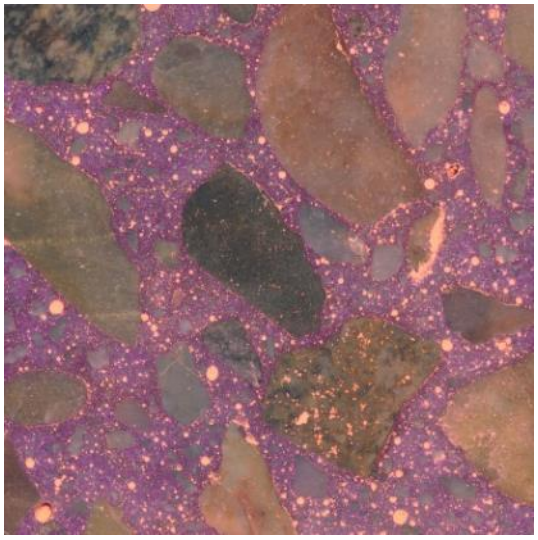

Figure B.37: Scanned photo, F3.

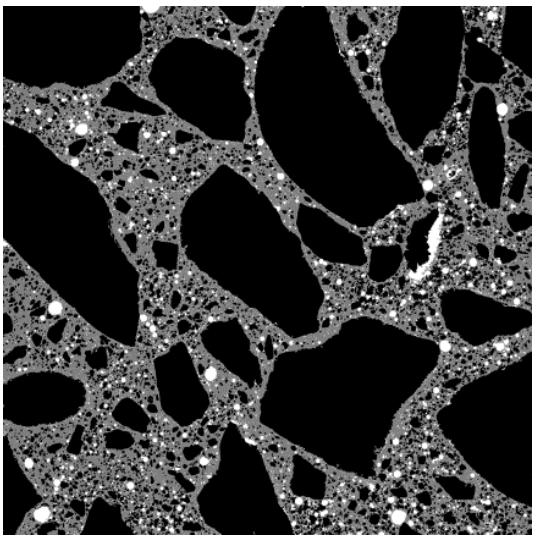

Figure B.38: Three-phase image, F3.

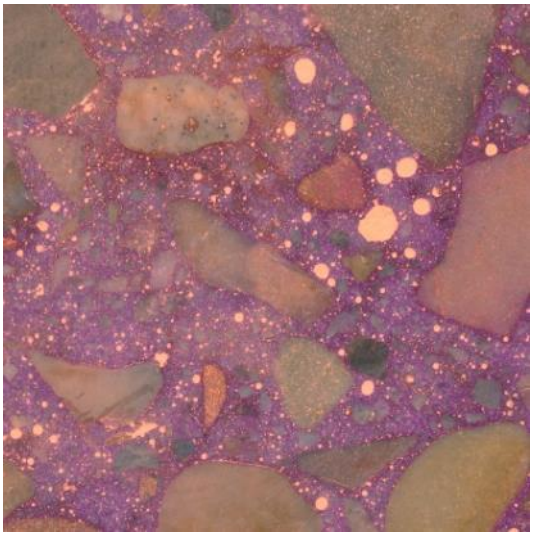

Figure B.39: Scanned photo, F4.

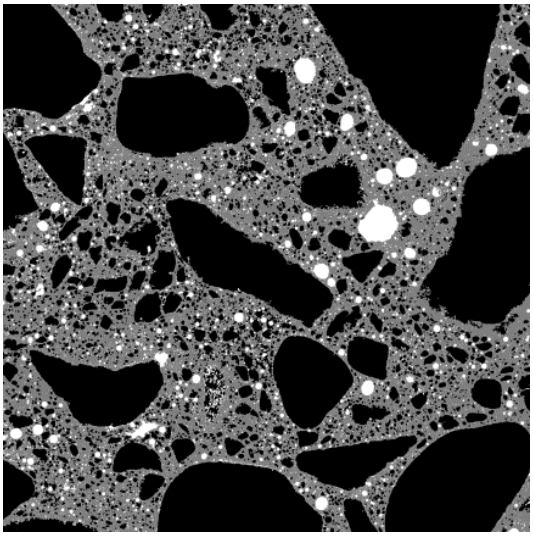

Figure B.40: Three-phase image, F4.

Appendix C. Cumulative Relative Frequency of the Average Distance

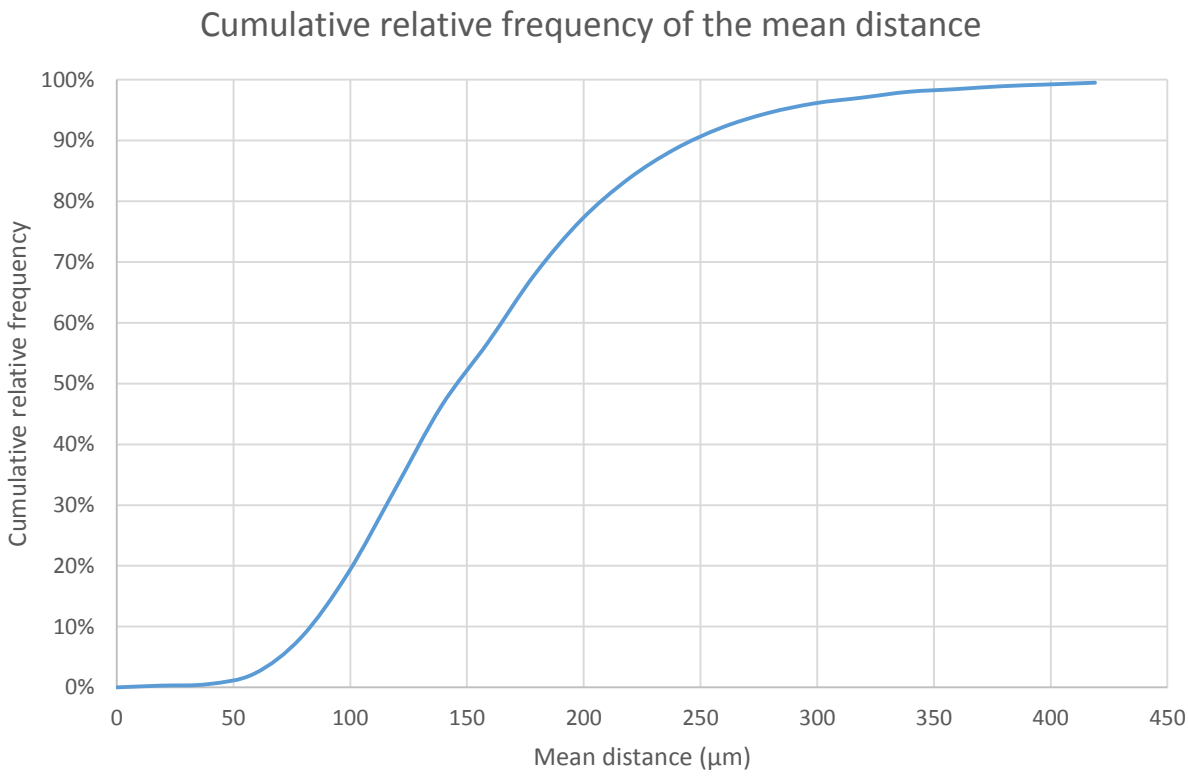

Figure C.1: Cumulative relative frequency of the average distance of A1.

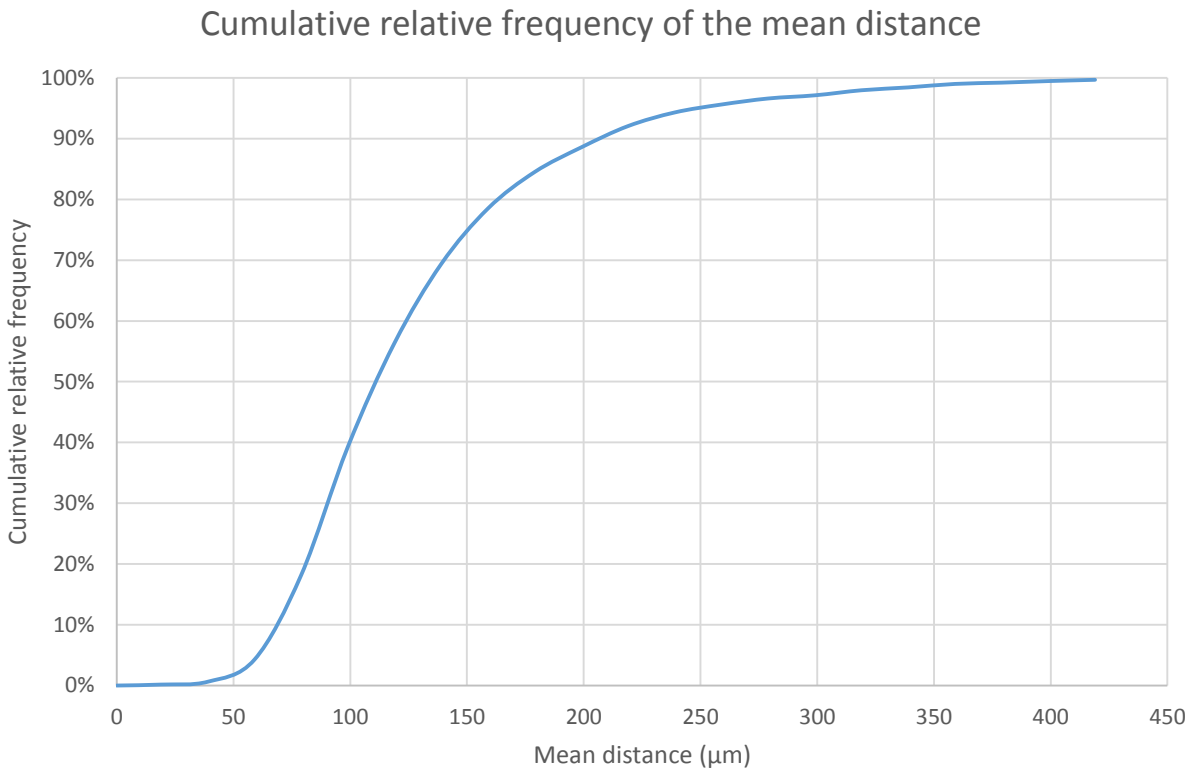

Figure C.2: Cumulative relative frequency of the average distance of A2.

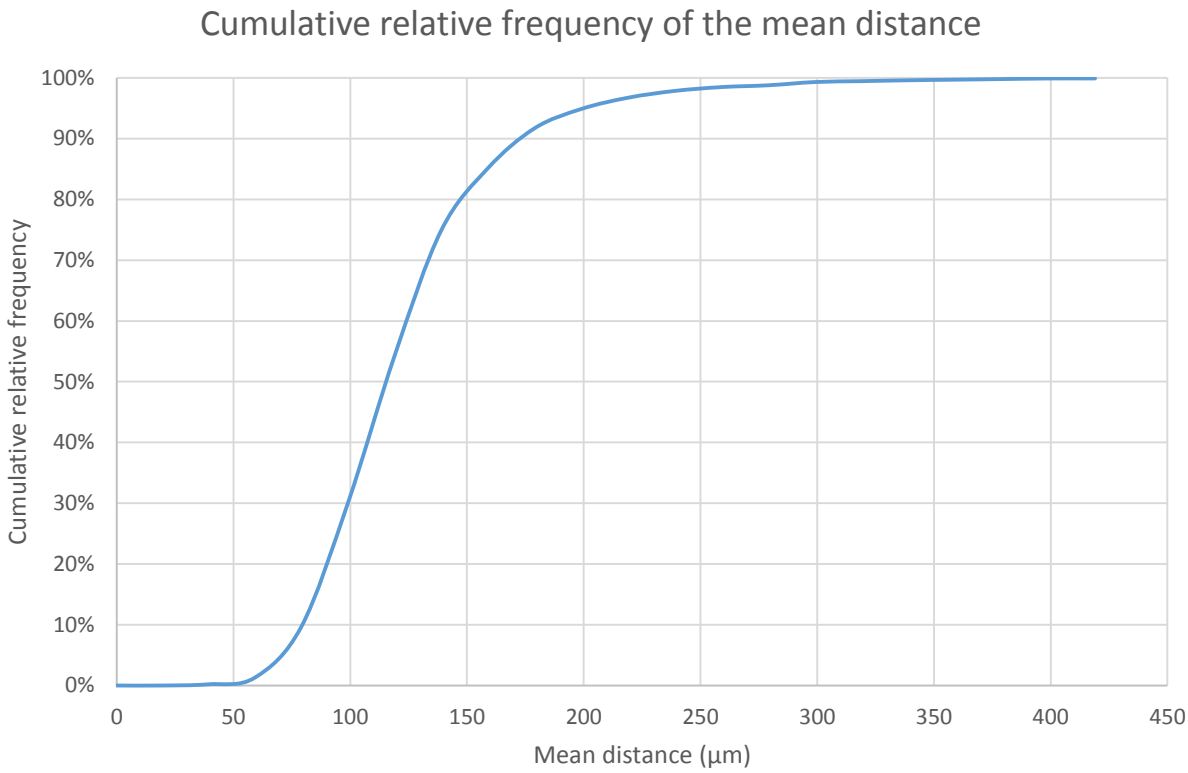

Figure C.3: Cumulative relative frequency of the average distance of A3.

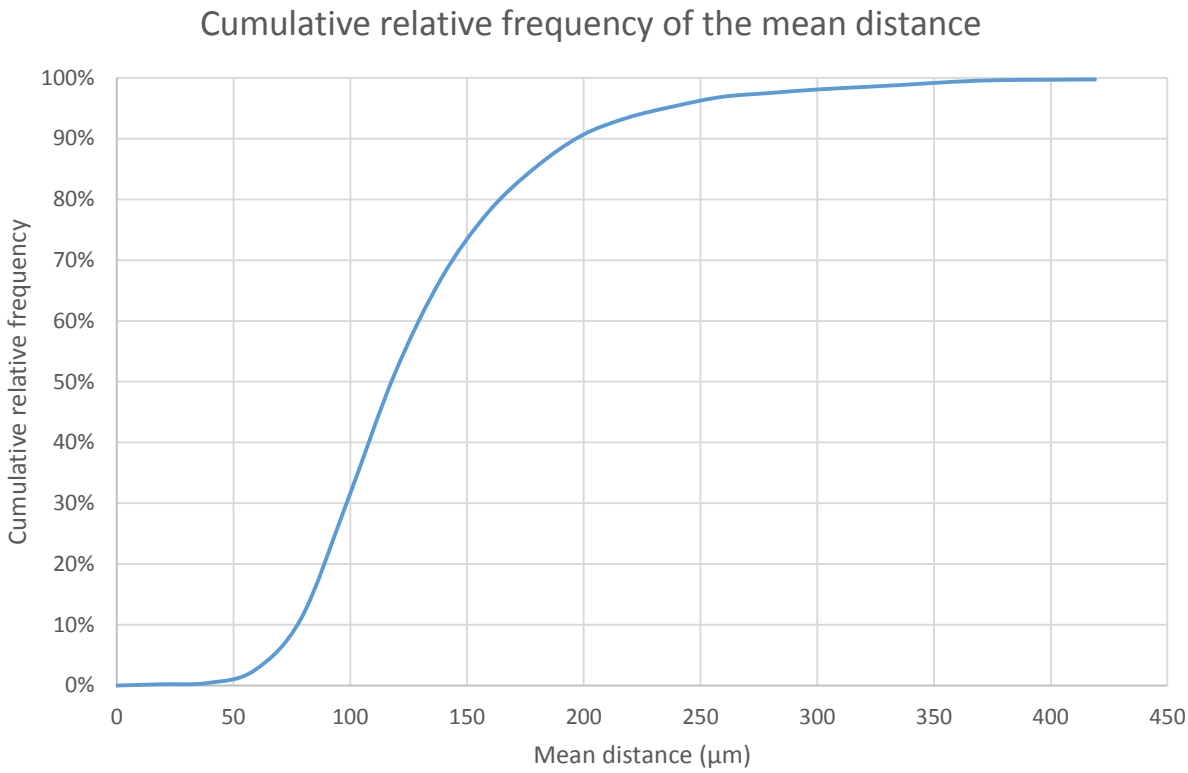

Figure C.4: Cumulative relative frequency of the average distance of A4.

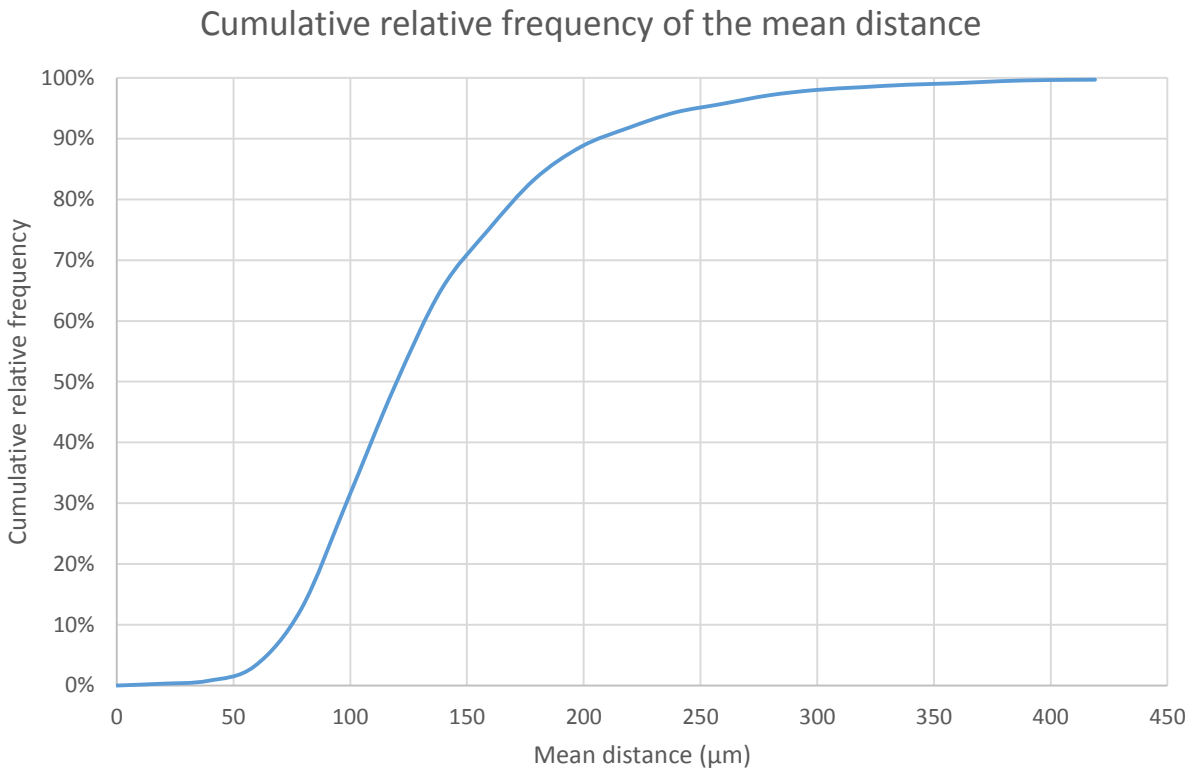

Figure C.5: Cumulative relative frequency of the average distance of B1.

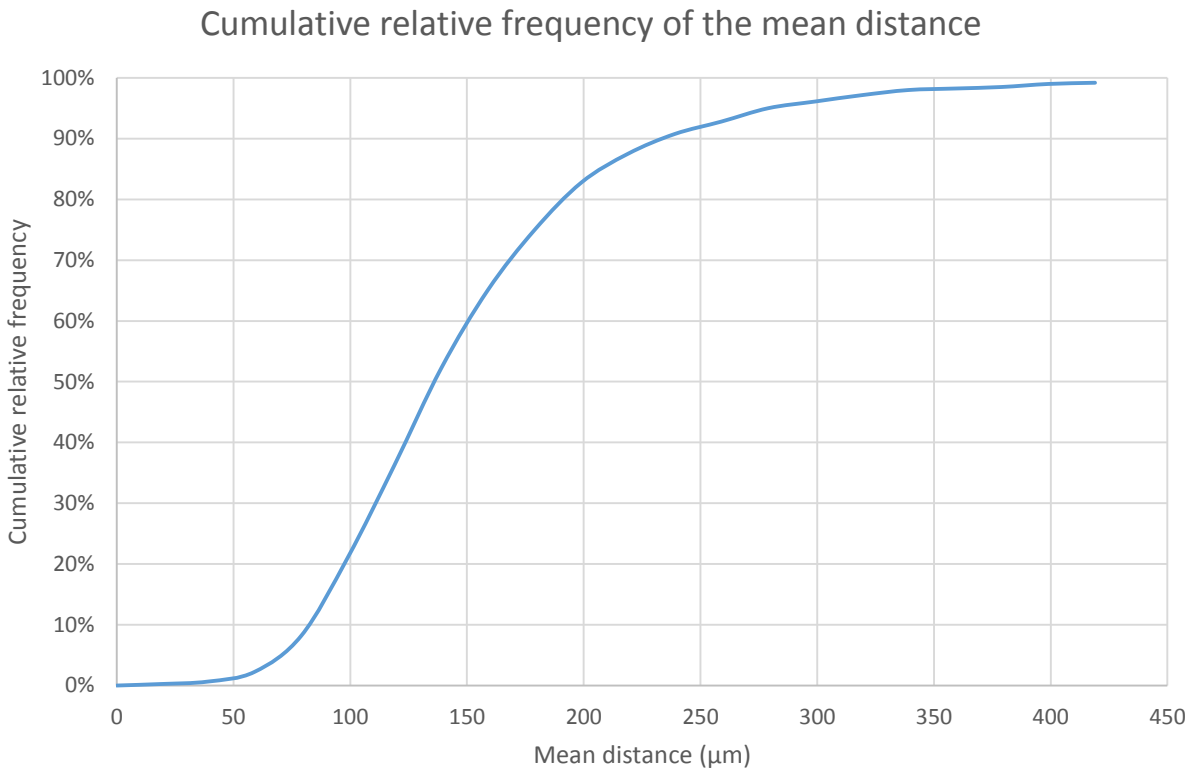

Figure C.6: Cumulative relative frequency of the average distance of B2.

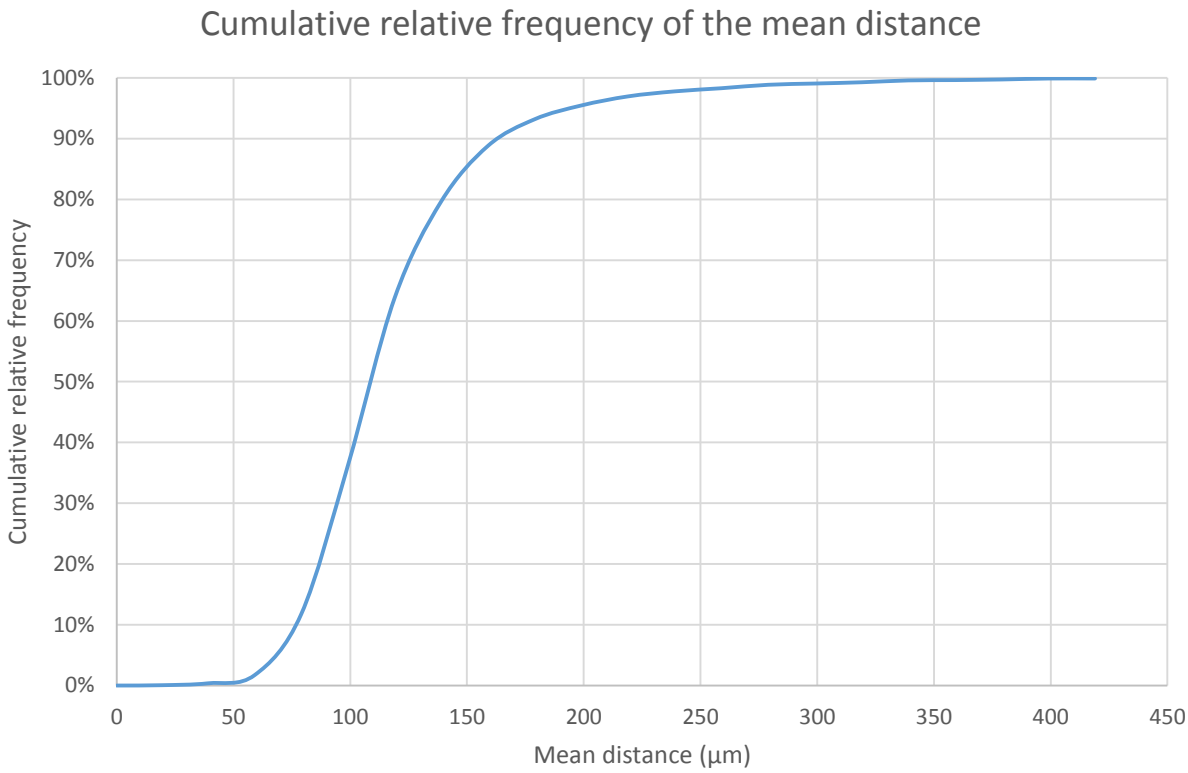

Figure C.7: Cumulative relative frequency of the average distance of B3.

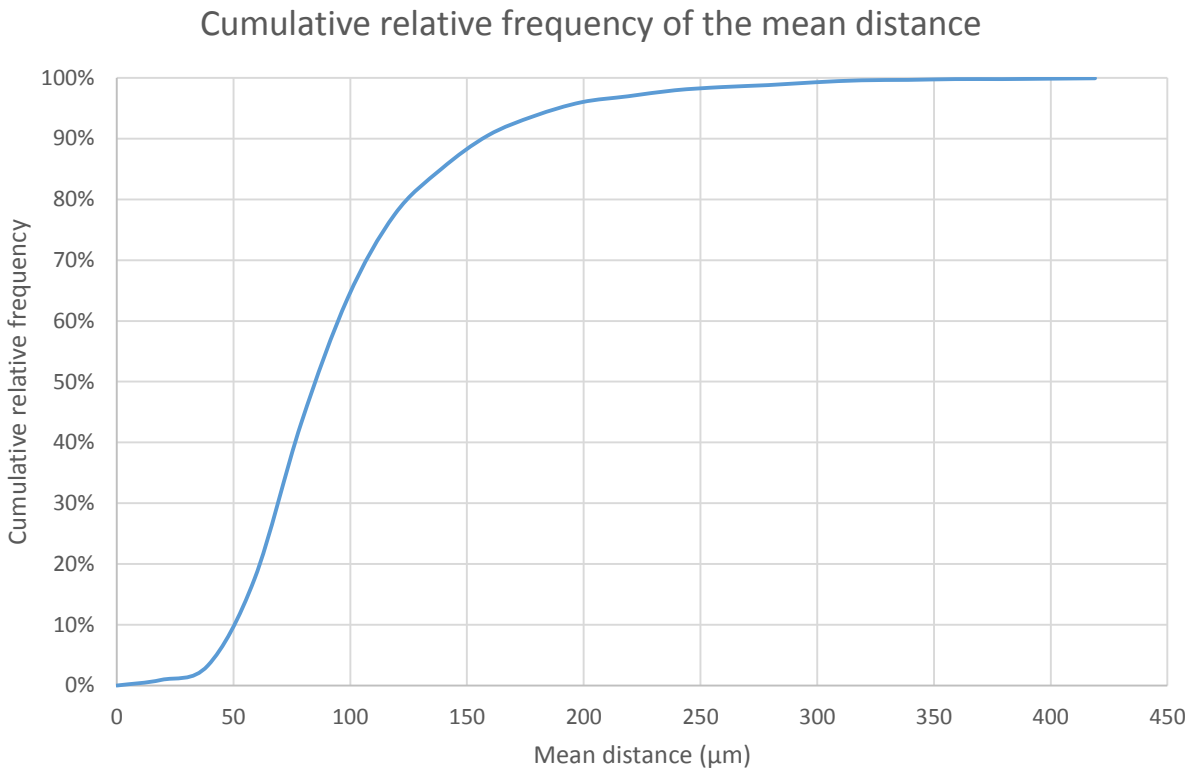

Figure C.8: Cumulative relative frequency of the average distance of E1.

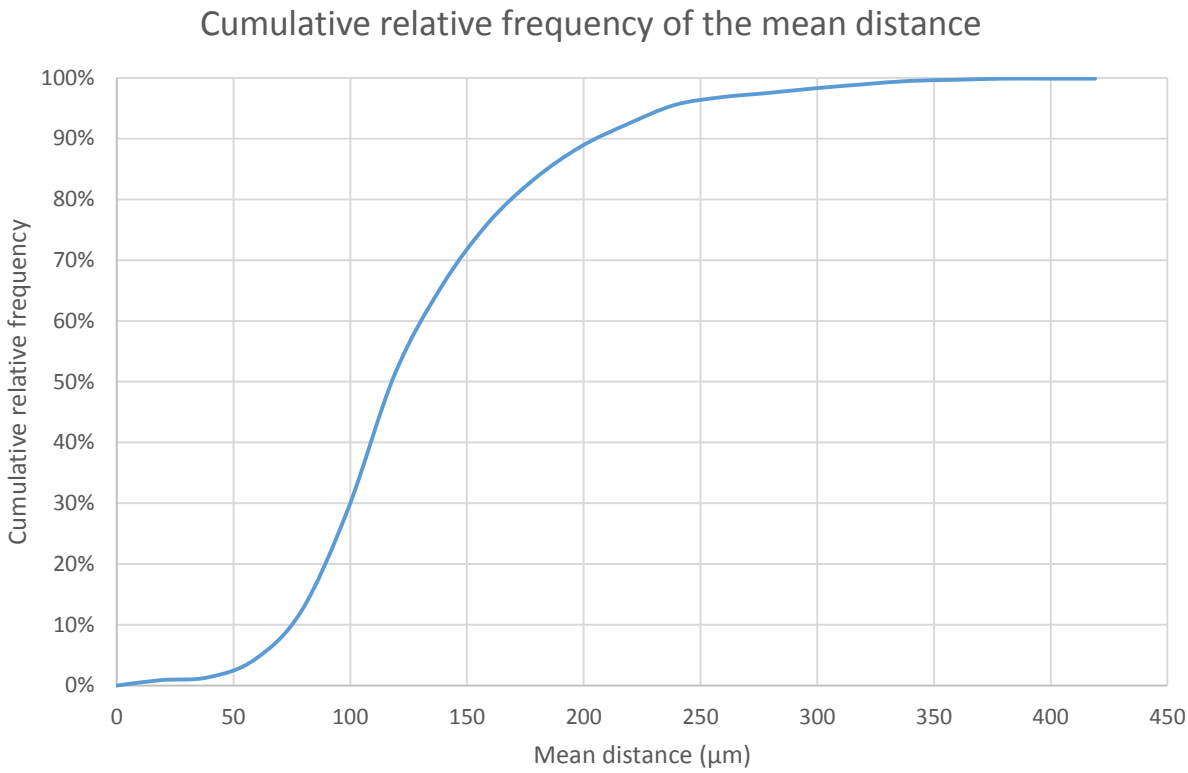

Figure C.9: Cumulative relative frequency of the average distance of E2.

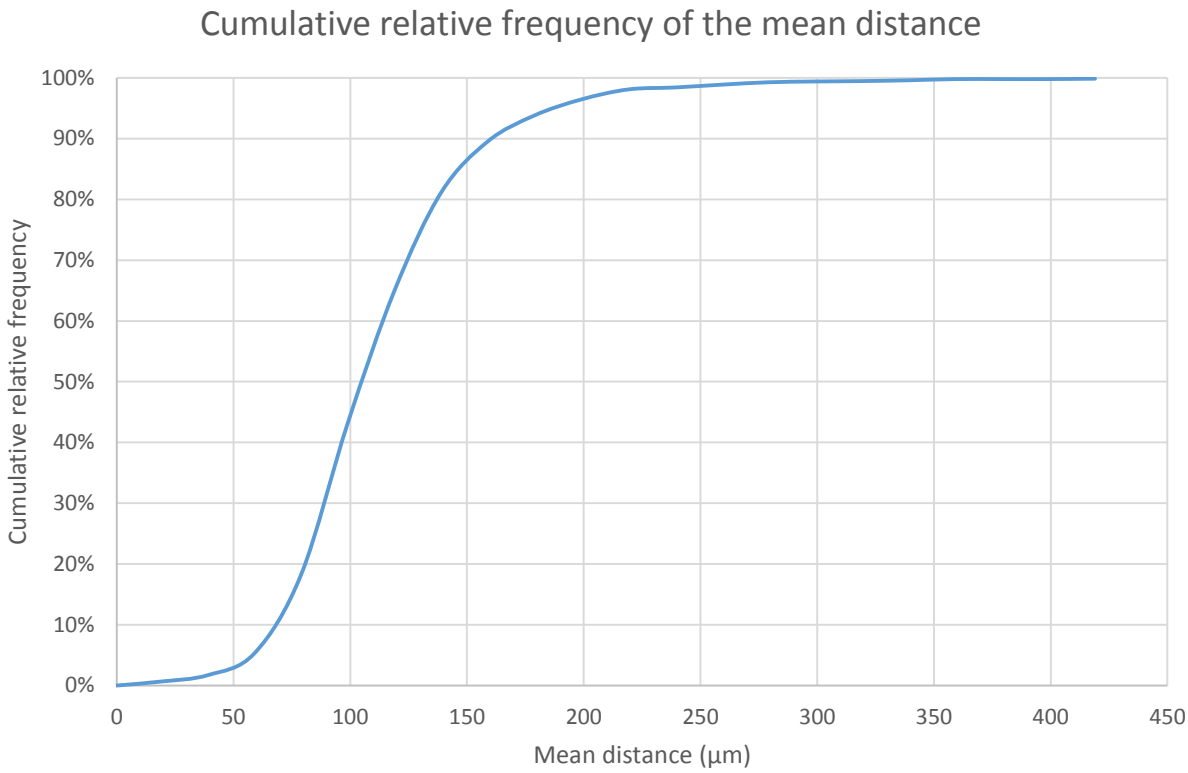

Figure C.10: Cumulative relative frequency of the average distance of E4.

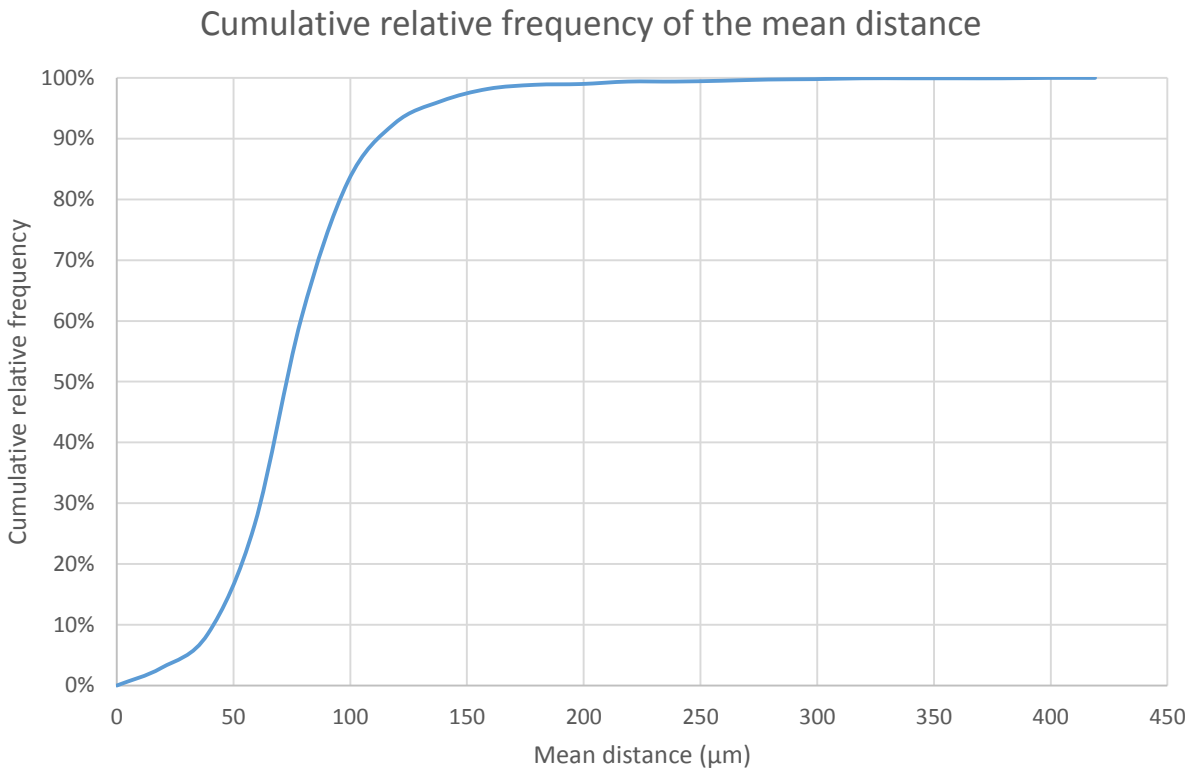

Figure C.11: Cumulative relative frequency of the average distance of F1.

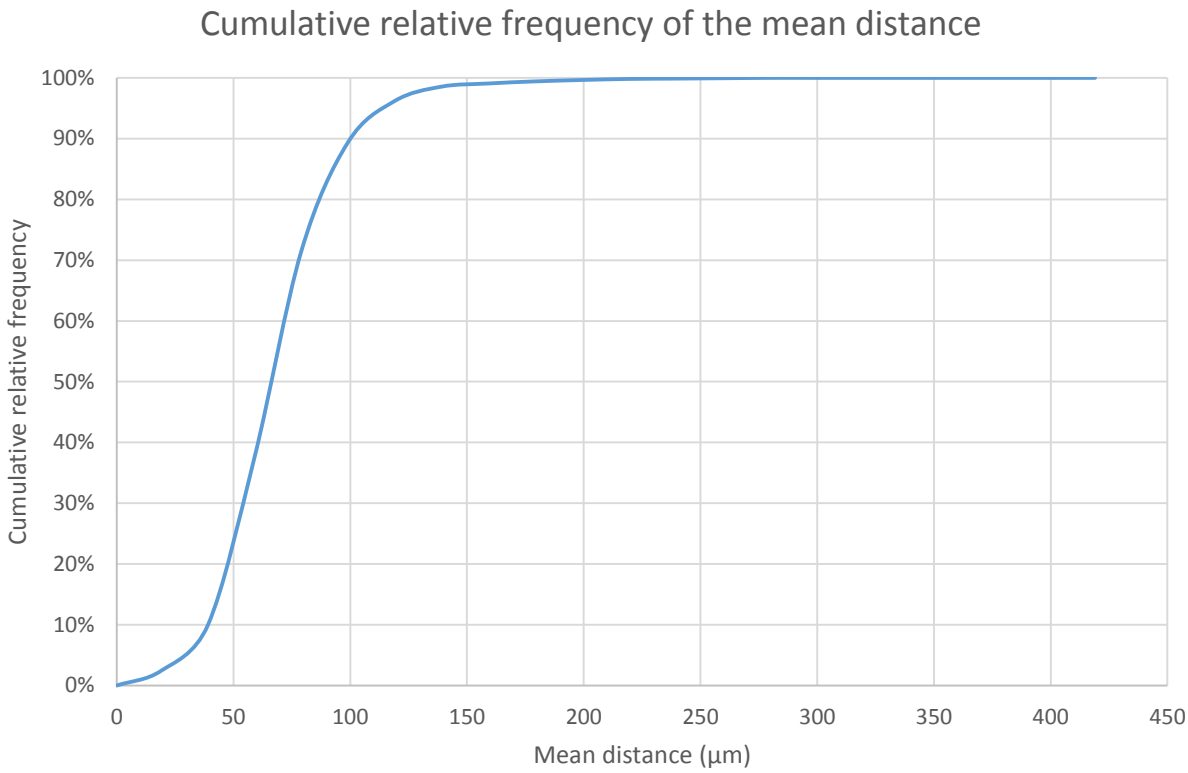

Figure C.12: Cumulative relative frequency of the average distance of F2.

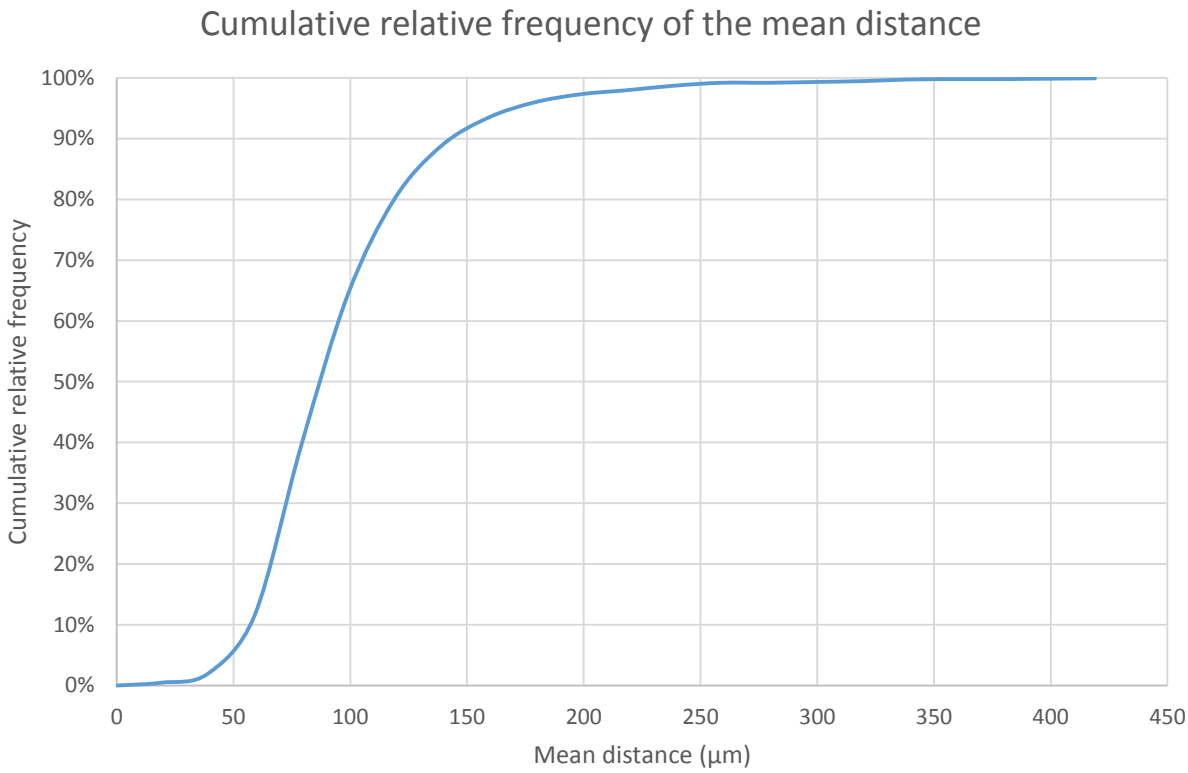

Figure C.13: Cumulative relative frequency of the average distance of F3.

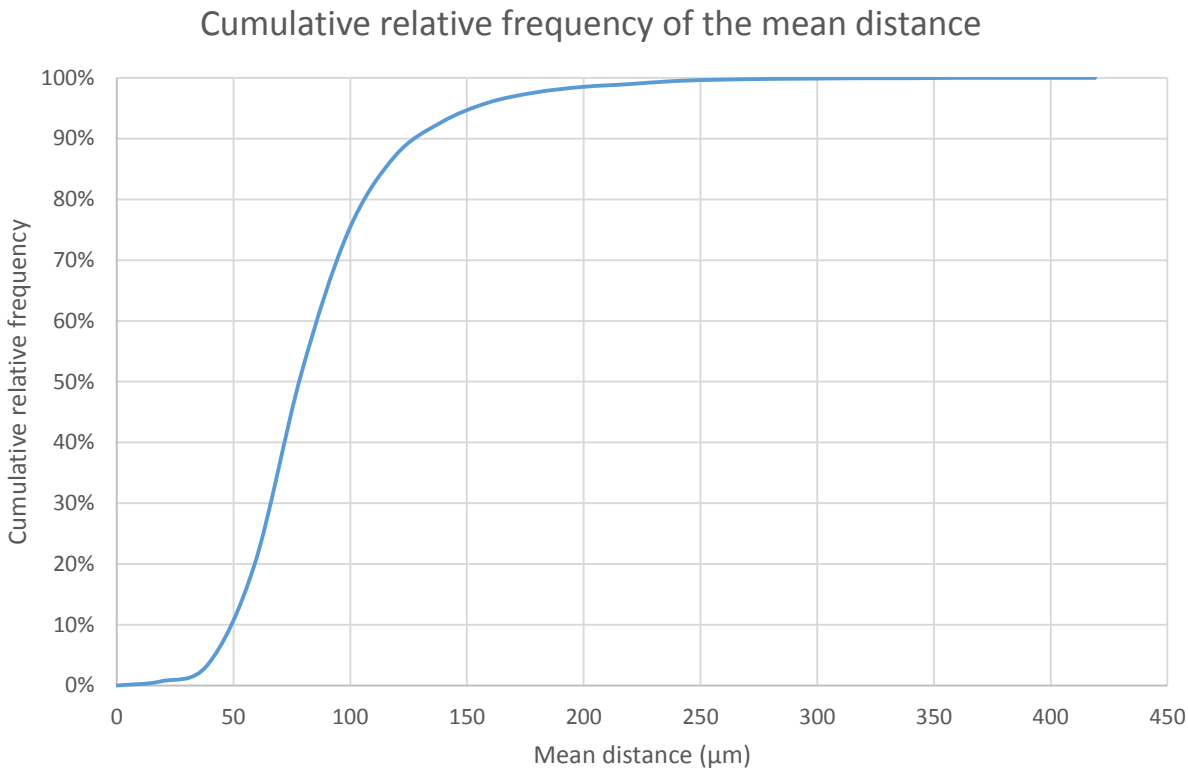

Figure C.14: Cumulative relative frequency of the average distance of F4.